VRIJE
UNIVERSITEIT
BRUSSEL

Thesis submitted with the goal of achieving a Master in Physics and Astronomy

INVESTIGATION OF THE PRECURSOR PHASE OF GAMMA-RAY BURSTS

Quinten Goens

June 5, 2019

Promotor Prof. Dr. Nick Van Eijndhoven
Supervisor Paul Coppin

Sciences and Bio-Engineering

Abstract

High-energy neutrinos are promising cosmic messengers which can advance our understanding of the physics involved in the most extreme astrophysical phenomena and environments in the Universe. The IceCube Neutrino Observatory has recorded numerous astrophysical neutrinos and is pursuing to identify the origin of these messengers by combining the available multi-messenger observations. However, up until now, no significant correlation has been found between detected neutrinos and Gamma-Ray Bursts (GRBs), which are among the most energetic events in the Universe. There has been extensive GRB research throughout the years and specialized detectors, e.g. the currently operational Fermi Gamma-Ray Space Telescope, have been built to examine this kind of transient short-lived bursts. The search for GRB neutrinos has mainly been focused on a temporal window overlapping with the prompt gamma emission phase of the GRB. This has been done through, for example, the combination of data observed by IceCube and Fermi. In this thesis the light curves of high-energy GRB emission will be examined, specifically focusing on the precursor phase of GRBs, with the goal to identify a wider search window for GRB neutrinos. A brief overview of the current state of multi-messenger astronomy and the detectors will be given alongside a theoretical overview of Gamma-Ray Bursts with a specific focus on the precursor phase.

Contents

List of Abbreviations

1M2H One-Meter Two-Hemispheres

ACD Anti-Coincidence Detector

BATSE Burst And Transient Source Experiment

BH Black Hole

BNS Binary Neutron Star

CsI Caesium Iodide

CTTE Continuous Time-Tagged Events

DOM Digital Optical Module

Fermi Fermi Gamma-Ray Space Telescope

GBM Gamma-ray Burst Monitor

GCN Gamma-ray Coordinates Network

GRB Gamma-Ray Burst

IAU International Astronomical Union

IC Inverse Compton

LAT Large Array Telescope

LIGO Laser Interferometer Gravitational-wave Observatory

MAGIC Major Atmospheric Gamma Imaging Cherenkov (Telescope)

NaI Sodium Iodide

NS Neutron Star

PHA Pulse Height Analysis

PMT Photo Multiplier Tube

SN Supernova

TTE Time-Tagged Events

UHECR Ultra-High-Energy Cosmic Ray

List of Figures

1 Introduction

For several decades ultra-high-energy cosmic rays (UHECRs)[1] have been observed. However, to date, their sources remain unknown. One of the plausible candidates are extremely energetic Gamma-Ray Bursts (GRBs). Under this hypothesis, neutrinos will also be produced in pγ interactions in these sources. As cosmic rays are charged, their paths are deflected by galactic and intergalactic magnetic fields, making it impossible to deduce their direction of origin. Neutrinos, however, travel unimpeded through the Universe and thus disclose their source direction. Multi-messenger observations of high-energy neutrinos and γ-ray photons from a GRB would provide confirmation of the hadronic interactions in GRBs and provide strong evidence for their role in UHECR production [1].

Gamma-ray bursts are the most luminous outbursts of electromagnetic energy in the Universe and are observed by specialized spacecraft (e.g. in the past by BeppoSAX and BATSE, currently by Swift and Fermi) at an average rate of approximately one per day. The observed γ-ray lightcurves of the prompt phase of GRBs are very diverse and have durations of several milliseconds to tens of minutes. A prevailing theory to describe this phenomenology is the fireball model, which entails a relativistically expanding fireball of electrons, photons and protons [2, 3]. The accelerated, high-energy protons in this fireball will interact with γ-rays emitted by electrons to create neutrinos through e.g. the delta-resonance

$$p + \gamma \rightarrow \Delta^+ \rightarrow \pi^+ + n \rightarrow e^+ + \nu_e + \bar{\nu}_\mu + \nu_\mu + n. \tag{1}$$

To date, no significant neutrino signals originating from GRBs have been detected across various searches in data from multiple years of AMANDA (IceCube's predecessor), ANTARES [4] or the completed IceCube detector [5].

A recent all-sky search in 2017 for the three flavours of neutrinos from GRBs has been conducted by the IceCube Neutrino Observatory examining 1172 GRBs. In this study no significant correlation between neutrinos and GRBs has been found, so tight constraints on neutrino and UHECR production mechanisms in GRBs have been set on the prompt phase of GRBs [5].

The temporal window to search for GRB neutrinos in these studies was set during the prompt gamma emission phase of the GRB. Therefore, in this thesis, an extension of this window during the precursor phase of GRB is examined based on GRB γ-ray emission observed by Fermi. The precursor phase of GRBs might be promising for neutrino production, as will be outlined later on.

[1] Cosmic rays with energies greater than 10^{18} eV.

1.1 Multi-Messenger Astronomy

Various branches in the field of astronomy have developed throughout the years with each of these observing a subset of the available signals or messengers from astronomical events. The best-studied observations are those of electromagnetic radiation or photons, which offer a wide range of complementary observations in different wavelengths (radio, infrared, optic, ultra-violet, x-ray and γ-rays). Other available messengers are cosmic rays, gravitational waves and neutrinos. Each of these messengers is observed by different means and they reveal complementary information about the (astro)physical processes taking place in the corresponding cosmic sources.

The goal of multi-messenger astronomy is thus to observe phenomena with different observatories optimized for specific messengers to enable the combination of all information available from the different fields. This aids to create a better understanding of the underlying physics as it allows to eliminate models or to create new models for these astronomical phenomena. To spread the information about significant events observed by one of the observatories, dedicated networks have been set up. The recent successes in the joint detection of multiple messengers have ushered in a new age of multi-messenger astronomy.

One of these successes was achieved on the 17th of August 2017, when the Fermi Gamma-ray Burst Monitor (GBM) classified a GRB (GRB 170817A) based on γ-ray observations and issued a notice to the Gamma-ray Coordinates Network (GCN). The GRB was observed at 12:41:06 UTC. Approximately six minutes after the GCN notice was issued a gravitational-wave candidate (GW 170817) was announced based on the single-detector analysis of the Laser Interferometer Gravitation-wave Observatory (LIGO) Hanford data. From the analysis, it was deduced that the phenomenon was a binary neutron star (BNS) merger with the time of merger 12:41:04 UTC (1.7 seconds before the GRB observation). Given the temporal and spatial coincidence of the two observations (by the GBM and LIGO) a follow-up GCN Circular was issued at 13:21:42 UTC for this highly significant candidate consistent with a BNS coalescence. GCN Circulars are notices for multi-messenger follow-up observations. Different radiation wavelength observations were made by ground- and space-based optical, radio, x-ray and γ-ray telescopes. A bright optical transient corresponding to this event (at the time identified as SSS17A; now with IAU identification AT2017gfo) was observed and localized to be in the galaxy NGC 4993 at a distance of approximately 40 Mpc by the One-Meter Two-Hemispheres (1M2H) Collaboration about eleven hours after the merger [6].

Another major success in multi-messenger astronomy was achieved by a cooperation between the IceCube Neutrino Observatory, the Fermi Large Array Telescope (LAT) and the Major Atmospheric Gamma Imaging Cherenkov (MAGIC) telescope collaborations. On the 22nd of September 2017, a neutrino-induced track was detected in the IceCube

Neutrino Observatory. The energy deposited by the track was $\sim$ 24 TeV, leading to a neutrino energy of $\sim$ 290 TeV. Subsequently, an automatically generated alert was distributed worldwide in a time span of only one minute to enable multi-wavelength searches by telescopes. Six days later, on the 28th of September 2017, the Fermi Large Area Telescope collaboration announced that the direction of origin of the neutrino (within $0.1°$) corresponded to the location of a catalogued blazar (TXS 0506+056, z=0.34). At the moment of neutrino detection, the blazar was in an active state with increased GeV γ-ray emission. Multi-messenger follow-up observations by the MAGIC observatory have revealed that γ-rays up to 400 GeV have been produced during certain periods of activity of the blazar. A subsequent analysis investigating the correlation between the neutrino and γ-ray production has a significance exceeding three standard deviations. The observed photon and neutrino energies indicate that blazar jets could be capable of accelerating cosmic rays to PeV energies since the neutrino energy is typically only about 4% of the energy of the parent cosmic ray particle. This correlation of high-energy neutrino production during a period of increased γ-ray emission in blazars indicates that blazars might be sources of very-high-energy cosmic rays and thus could be the phenomenon responsible for a fraction of the cosmic neutrino fluxes observed by the IceCube Neutrino Observatory [8].

According to the Hillas criterion [12], which relates the maximum cosmic-ray energy of a source to its size and magnetic field strength, there is another potential source of very-high-energy neutrinos and high-energy cosmic rays, namely Gamma-Ray Bursts (GRBs). This is illustrated in the Hillas-plot in Fig. 1. The Hillas criterion is a general geometrical criterion, which is useful in selecting potential acceleration sites. It is based on the idea that if a particle escapes the acceleration region, it will no longer be able to gain more energy. This imposes a limit on the maximum energy ϵ_{max}, which can be expressed as

$$\epsilon_{max} = qBR, \tag{2}$$

where q is the electric charge of the particle, B is the strength of the magnetic field and R is the size of the accelerator. This equation (eq. (2)) is obtained by demanding that the Larmor radius of the particle, $R_L = \epsilon/(qB)$ does not exceed the size of the accelerator region [9].

GRBs are among the most energetic and luminous phenomena in the universe. They release massive amounts of high-energy radiation in extremely short timespans [10]. To support the assumption that GRBs could be the source of very-high-energy neutrinos it would be important to simultaneously observe neutrinos and γ-rays from these transients as this would allow us to identify them as sources of the cosmic neutrinos detected by IceCube as well as the sources of the UHECRs detected by the Auger and Telescope Array observatories. However, up until now no significant correlations between signals have been found. As these bursts are very short-lived and not completely understood, one might argue on whether one should widen the neutrino search window beyond the usual γ-ray prompt emission burst period, as up until now no neutrinos have been observed during the prompt gamma emission phase of a GRB with a high significance [11]. Examining the temporal spectrum of high-energy GRB emission, specifically focusing on the precursor phase of GRBs, with the goal to identify a wider search window is the aim of this thesis.

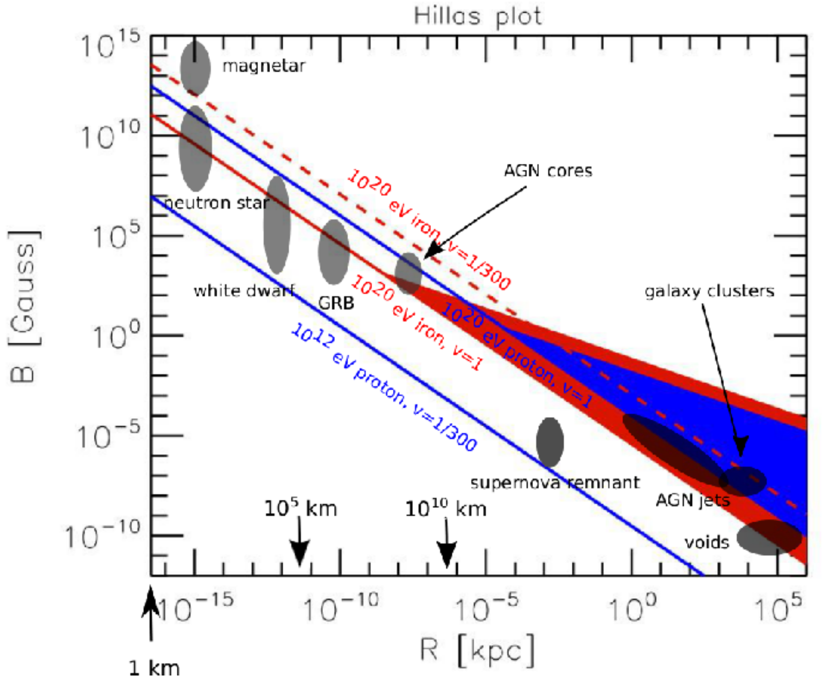

Figure 1: The Hillas diagram which displays the possible cosmic-ray accelerators for various energies based on the theoretical models of their magnetic fields and radii [12].

1.2 The Fermi Gamma-Ray Space Telescope

The Fermi Gamma-Ray Space Telescope (Fermi) has been launched into orbit on the 11th of June 2008 and started its first observations on the 11th of August 2008. Since its launch, the telescope is located in a low-Earth circular orbit. It is at an altitude of $\sim$565 km and at an inclination of 25.6 degrees with respect to the Earth's equatorial plane. There are two main components to Fermi, the Large Area Telescope (LAT) and the Gamma-ray Burst Monitor (GBM). The former, the Large Area Telescope, is the primary element of Fermi. It is a wide field-of-view (about 60° from the instrument axis, covering about 20% of the sky) pair-conversion telescope, which makes observations of photons in an energy range from 20 MeV to about 300 GeV. The latter, the Gamma-ray Burst Monitor, is sensitive to energies between 8 keV and 40 MeV. The GBM has a larger field of view than the LAT and as such is very efficient in detecting transient phenomena. It detects more than 200 GRBs per year whereas the LAT only observes $\sim$12 GRBs per year [13].

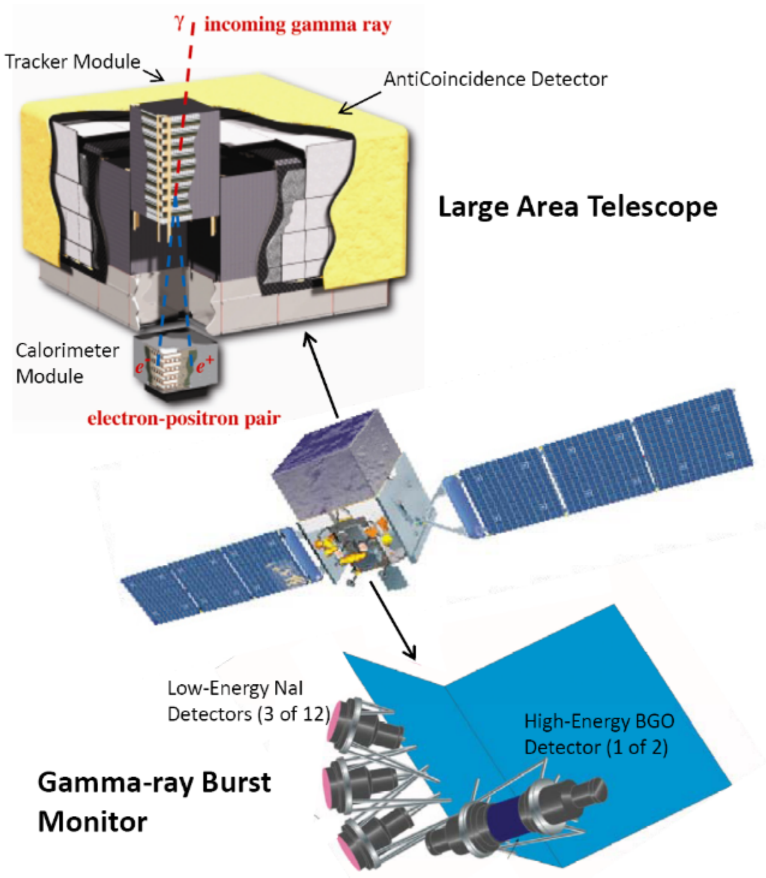

Figure 2: An illustration displaying the setup of the Fermi Gamma Ray Telescope [13].

Since high-energy γ-rays cannot be reflected or refracted, a high-energy γ-ray in the detector is detected by conversion into an $e^{+}e$ pair. The LAT makes use of this pair-conversion by the usage of a precision converter-tracker section followed by a calorimeter. These subsystems are made up of a 4×4 array of 16 modules as can be seen in Fig. 2. The tracker consists of silicon-strip detectors. The combined signals induced in several layers of the tracker allow for the determination of the path of the particles. The calorimeter is a hodoscopic configuration of ~ 8.6 radiation lengths[2] of caesium iodide (CsI) crystals which enable the measurement of the total energy of the particles. These instruments allow for the imaging of the shower development in the calorimeter as well as for correcting the energy estimate for shower leakage fluctuations out of the calorimeter. The thickness of the whole system (tracker and calorimeter) is about 10 radiation lengths at normal incidence. The third subsystem in this detector is the segmented anti-

[2] A radiation length is a characteristic property of a material and describes the energy loss of high-energy particles by electromagnetic interactions with the material. A radiation length is the mean length needed to reduce the energy of a high-energy electron by a factor of $1/e$ [14].

coincidence detector (ACD), which covers the tracker array. This system is designed to reject the majority of charged particles entering the detector as they are background signals for the γ-ray detections. The subsystems combine to produce a programmable trigger and data acquisition system which uses prompt measurements from the tracker, calorimeter and ACD. This in order to create a trigger that initiates read-out of these three subsystems. The onboard trigger mechanism will reject events which are triggered by background particles, such as cosmic rays [15].

The Gamma-ray Burst Monitor (GBM) consists of twelve relatively low energy thallium doped sodium iodide (NaI(Tl)) detectors (from 8 keV to 1 MeV) and two high-energy (from 200 keV to 40 MeV) bismuth germanate (BGO) detectors. The GBM can be seen in Fig. 2. The detectors are mounted at opposite sides of the telescope and each of the detectors is unshielded. They are uncollimated scintillators of which the location and orientation are composed in such a way that each one has a different viewing angle. This allows to determine the direction of a burst by making a comparison of the count rates and timing for each detector. After the GBM detects and determines the position of an event, it communicates it on-board to the LAT. If a burst exceeds a pre-set threshold, the craft will autonomously rotate to keep the GRB within the LAT field-of-view for the coming 5 hours. This to optimize the temporally extended observation of high-energy γ-ray emission with the LAT [16].

The instrument of main interest for the current study is the Gamma-ray Burst Monitor, as the GBM observes more GRBs (> 200) than the LAT (~ 12) per year. Each signal observed by one of the Photo Multiplier Tubes (PMTs) in the detectors of the GBM is analyzed separately. The larger the energy deposit of an incoming photon, the larger the signal. If it is above a certain threshold, it will be classified as an event and the signal waveform will be recorded. This waveform is then binned into either eight or 128 predetermined bins as part of the Pulse Height Analysis (PHA) bins, which are based on lookup tables [16].

The GBM records its data in three types: CTIME, CSPEC and TTE. The CTIME data describes events into eight PHA bins and has a default temporal resolution of 256 ms. However, when a GRB is detected, the temporal resolution temporary increases to 64 ms. The second type of data, Time-Tagged Events data or TTE data, has 128 PHA bins and records the arrival time for every photon instead of using temporal binning. About 30 seconds of TTE data is continuously buffered and saved if a GRB trigger occurs. Since an update on the 26th of November 2012, continuous TTE (CTTE) data has been available during normal spacecraft operations. Lastly, the CSPEC data is also binned in 128 PHA bins and has a default temporal resolution of 4.096 seconds. However, after GRB detection this temporal resolution increases to 1.024 seconds [16].

GRB detection by the GBM happens onboard and in real-time. A GRB trigger occurs when at least two NaI detectors record a photon rate increase above a threshold. This threshold is adjustable for observing different transient phenomena and is specified in units of the standard deviations above the background rate. This background rate is the average rate over a previous period (during normal operations this is 17 seconds). To accommodate the detection of various transient phenomena different triggering algorithms are in place for different energy and time ranges. A GRB trigger prompts the GBM to transmit TTE data to the spacecraft, the transmitted data, obtained from a temporary storage buffer, starts 30 seconds before the trigger and ends ~300 seconds after the trigger. After the trigger, the CTIME and CSPEC temporal resolutions are increased to 64 ms and 1.024 s respectively for $\sim$ 600 seconds. The localization of the GRB after the trigger is performed onboard by comparing relative rates and timing in the NaI detectors to the lookup tables and typically has a statistical angular uncertainty of 3° [16].

For the current study, the main interest is in observing the structure of the light curves of GRBs and its precursors. Therefore the high temporal resolution as found in the CTIME data or the time-tagged event (TTE) data is favoured above the CSPEC data for this analysis.

1.3 The IceCube Neutrino Observatory

The IceCube Neutrino Observatory, located in Antarctica near the Amundsen-Scott South Pole Station, is the first ice based high-energy particle detector of its kind. The main goal of the observatory is to detect high-energy neutrinos and to investigate their sources. The study of these neutrinos might also shed some light on the nature of dark matter and provide information about the properties of the neutrinos itself [21]. The IceCube Collaboration consists of an international team of approximately 300 physicists from 48 institutions in 12 different countries conducting scientific research around these topics [17].

The observatory is embedded within a cubic-kilometre of the Antarctic ice (see Fig. 3). High-energy charged particles passing through a dielectric medium, such as ice, emit Cherenkov radiation if they are travelling faster than the speed of light itself in this medium. The Cherenkov radiation produced in this phenomenon is explained by the restoration of the medium by the de-excitation of electrons by the emission of photons. Light transversing this medium is slower than the charged particle, causing the emission to be cone shaped (see Fig. 4). The opening angle of this cone is called the Cherenkov angle θ_C and is specific for the medium since

$$\cos\theta_C = \frac{1}{n\beta}, \tag{3}$$

where n is the index of refraction and $\beta = v/c$. This Cherenkov angle is crucial in the track reconstruction of IceCube.

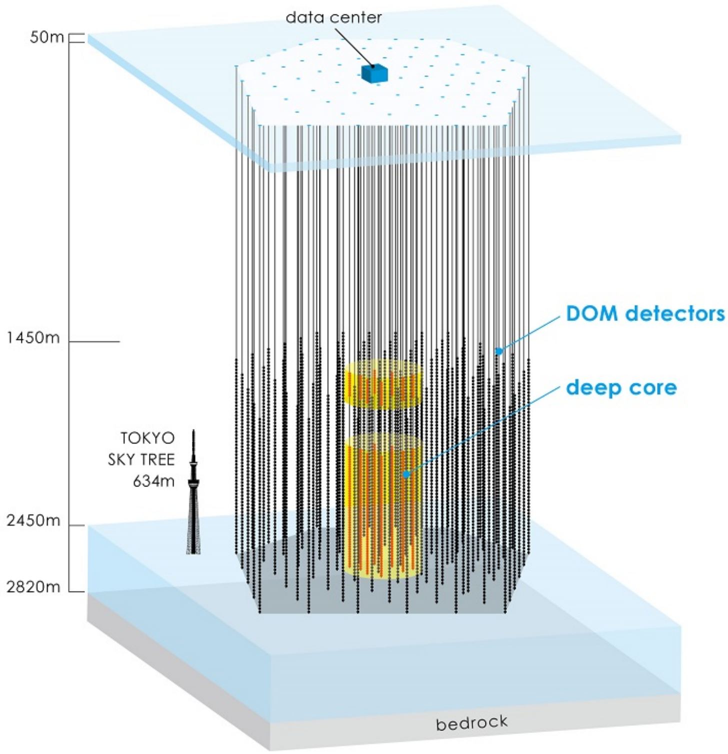

Figure 3: An illustration of the IceCube Neutrino Observatory and its subdetector DeepCore [20].

To detect this Cherenkov radiation, Digital Optical Modules (DOMs) containing photomultipliers are placed in the ice on 86 vertical strings [18, 21]. These vertical strings are positioned in a triangular grid with 125 meters horizontal spacing between different strings and each contains 60 DOMs vertically spaced by 17m. In the centre of the detector, a denser configuration with a horizontal string spacing of about 70m and a vertical DOM spacing of about 7m, called the DeepCore subdetector, has been deployed to lower the neutrino energy detection threshold from about 200 GeV to roughly 10 GeV. A reconstruction of the observed signal is performed based on the strength of the observed Cherenkov radiation, the recording times of the various DOM signals and the location of each DOM [22].

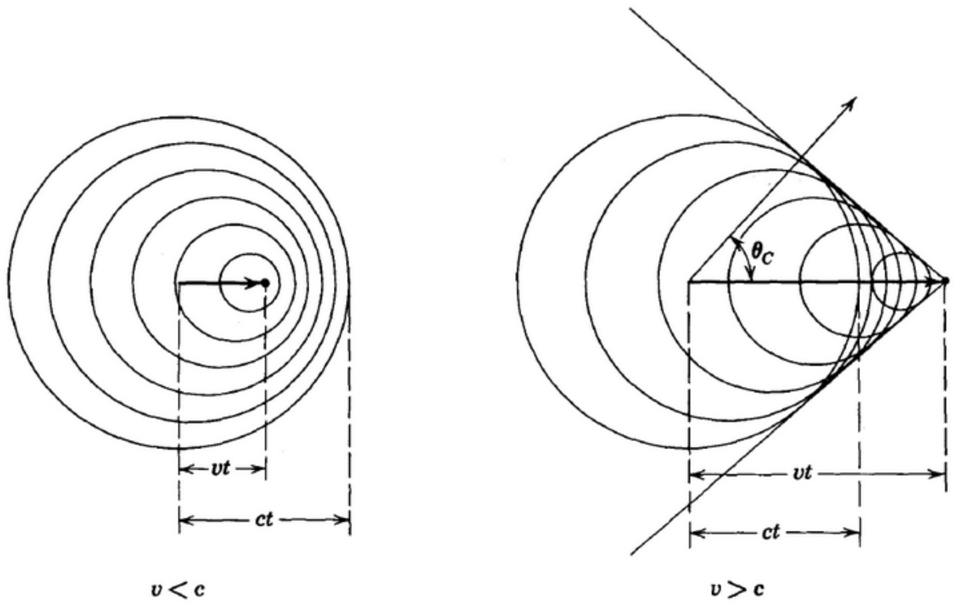

Figure 4: An illustration of Cherenkov radiation. Left: Spherical emission of radiation due to de-excitation of electrons in the surrounding medium with the velocity of the particle smaller than the speed of light in the medium. Right: Conical emission. The particle travels faster than the speed of light in the medium, leading to an electromagnetic shockwave. This shockwave travels in the direction of the Cherenkov angle θ_C [19].

The small neutrino cross-section, in general, prevents direct detection, as interactions with matter are unlikely. When a neutrino traverses a huge dense mass like the Earth, the interaction likelihood increases. As all neutrino flavours are electrically neutral, they will not produce Cherenkov radiation directly when traversing the polar icecap. However, when a charged current interaction occurs between an incident neutrino (ν_l) and an atomic nucleon in the ice (N), a charged lepton (l) corresponding to the flavour of the neutrino will be produced accompanied by a hadron shower (X)

$$\nu_l + N \to l + X. \tag{4}$$

For example, muon neutrinos arriving from the Northern Hemisphere can interact with nucleons from atomic nuclei in the Earth. A charged current interaction might occur,

$$\nu_\mu + N \to \mu + X, \tag{5}$$

where N is used to indicate a nucleon and X is a combination of other hadronic particles. This interaction can happen as well with the respective antiparticles (a muon anti-neutrino can produce an anti-muon) or the other neutrino flavours ν_e and ν_τ [19].

Due to the differences in properties, such as mass and lifetime of the charged leptons produced in the charged current interactions, each neutrino flavour will have a different signature in the detector depending on the type of interaction as illustrated in Fig. 5. Electrons are typically scattered multiple times before falling below the Cherenkov threshold due to their low mass. This prohibits using the observed signals to find a direction of origin of the neutrino. However, the interacting electron will be fully contained within the detector and can thus be used for energy studies. These type of roughly spherical signatures are called cascades. Another interaction that produces a cascade that may occur for all flavours is the neutral-current interaction, where the (anti-)neutrino scatters on atomic nuclei in the Earth without being transformed into the corresponding charged lepton, is

$$\nu_l + N \rightarrow \nu_l + X. \tag{6}$$

Another type of observational signature, a track, is typically caused by muons. The higher mass of the muon (compared to the electron) decreases energy loss via Bremsstrahlung and scattering and thus the penetration of muons through the ice is substantially higher. Muons can transit the entire detector, which is ideal to provide strong constraints on the neutrino direction of origin. However, as these tracks are not always completely contained within IceCube, the energy is not fully deposited within the detector and thus the energy of the muon and the primary neutrino remain uncertain [19].

To investigate the origin of the observed neutrinos, IceCube is mainly interested in detecting muon neutrinos. When a charged current interaction happens in the proximity of the detector, the produced muon will create a track. From the observation of the muon track, we can find the approximate origin of the neutrino since the angle between the path of the muon and the path of the neutrino is very small at high energies. The opening angle between the neutrino and the muon is about $1.5°/\sqrt{E}$ where E is the energy in TeV [25]. Alternatively, electrons produced in charged current interactions will cause an electromagnetic cascade from which it is harder to reproduce the point of origin. Tauons, on the other hand, have a short lifespan which makes them less ideal candidates to observe. Due to their short lifetime of 2.9×10^{-13} s, only extremely energetic tauons might produce a specific type of track in the detector called a "Double-Bang", where both the creation and destruction of the tauon are observed [26]. An overview of these signatures can be seen in Fig. 5.

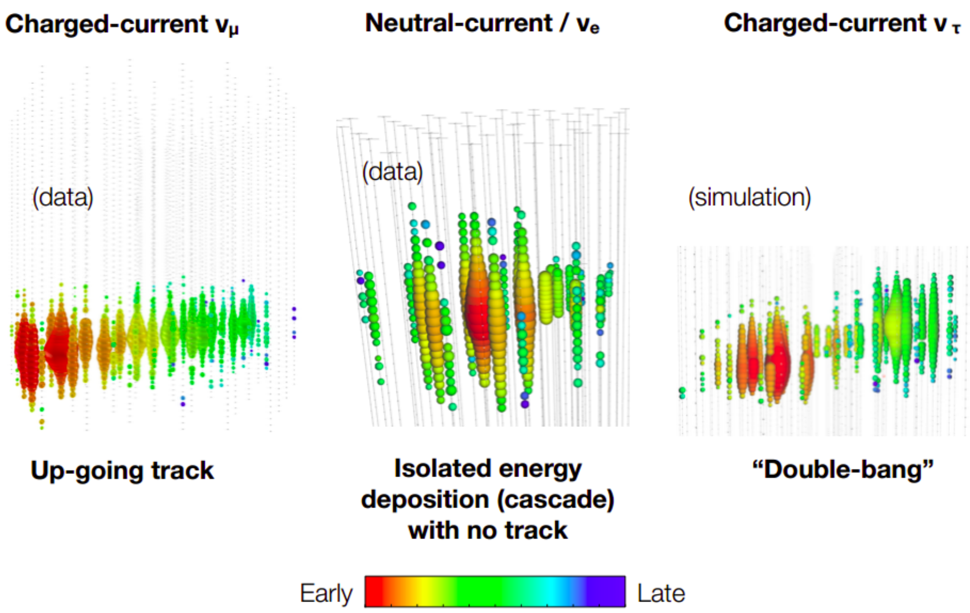

Figure 5: Left: A track induced by a negative or positive muon generated by either a charged current muon (anti)neutrino interaction or an air shower. Center: A cascade induced by either a charged current electron (anti)neutrino or a neutral current (anti)neutrino interaction. Right: A simulated representation of a Double Bang induced by a charged current tauon (anti)neutrino [20].

Part of the background detection is performed by IceTop. This is a subdetector of IceCube for the study of cosmic rays with 81 stations located at the surface, on top of the strings of DOMs embedded in the ice. These stations consist of two tanks filled with (frozen) water, each containing two DOMs facing down. High-energy cosmic rays entering the atmosphere in the Southern Pole region might generate secondary particles, such as muons, which will trigger the DOMs in the ice. As IceCube is aiming to detect high-energy neutrinos, these cosmic-ray background signals have to be removed and will thus be categorised as background. Neutrinos are non-charged, nearly massless and almost non-interacting and will pass through the Earth as opposed to charged cosmic rays. When these neutrinos possibly interact with nuclei in the Earth, a track or cascade might be detected by the DOMs. If signals are simultaneously detected by IceTop and IceCube, these will be vetoed as they likely originate from high-energy cosmic rays and not from neutrinos. These signals will be categorised as background for neutrino studies. However, the produced data is used for cosmic-ray studies [23].

There are multiple benefits for building the IceCube detector in the Antarctic ice. The Cherenkov radiation produced by the high-energy particles in the natural present ice enables us to observe and quantify the particle energies and determine a direction of origin. The detector is located 1450 to 2450 meter beneath the ice. Due to the attenuation of light by the ice above the detector, only a low (about 500 Hz) electronic background rate will be observed in the DOMs. Another benefit of this location is the upscale possibility of the detector. The next generation detector named IceCube-Gen2 is now being planned, taking advantage of this, and will cover a volume of about ten cubic kilometres. This should increase the statistics of the currently observed cosmic neutrinos and even allow reaching out to higher energies [24].

2 The Theory of Gamma-Ray Bursts

Gamma-Ray Bursts (GRBs) connect a plethora of different areas in astrophysics. These relativistic events are connected to the end stages of stars. They interact with the surrounding medium and due to their enormous energy output on relatively short timescales, their luminosity makes the event of great interest for cosmology. They emit not only high-energy radiation and possibly gravitational waves [28], but they are also expected to be a source of Ultra-High-Energy Cosmic Rays (UHECRs) [29, 30] and neutrino emission [31].

GRBs are unpredictable and non-repetitive. The emission of γ-rays occurs in violent flashes lasting from milliseconds to tens of minutes and comes from random directions in the sky. Assuming an isotropic energy output, a GRB is able to output an energy of about 10^{52} erg, which is comparable to the total energy the Sun will emit during its whole main-sequence lifetime. The spectrum is non-thermal with the bulk of emission falling in the 0.1 to 1 MeV range [32].

Studies of the light curves indicate that the violent event which causes the gamma-ray burst produces ultrarelativistic jets which beam the ejecta [33]. The interactions between the particles in the jets are capable of producing bright and rapidly varying prompt emission. They have been assumed to be the source of ultra-high-energy cosmic rays (which are cosmic rays with energies up to 10^{20}eV) according to the Hillas criterion [34]. However, recent research conducted by the IceCube Collaboration has placed strong limits on the likeliness of this claim. The model predicting the highest neutrino flux, in which cosmic ray protons escape the confinement of the GRB's magnetic fireball as neutrons whereafter they decay to protons has already been ruled out [5]. Other possible models are currently still being investigated with the aim of identifying GRB neutrinos and UHECR.

The jet's interaction with the external medium at about $10^{16} - 10^{17}$cm from the central engine can cause a long-lived fading afterglow emission. This emission appears as point-like sources in x-rays, ultraviolet, optical, infrared and radio wavebands. This is illustrated in Fig. 6. The afterglow fades away after a few hours to weeks, sometimes months. Observing this afterglow can reveal the surrounding host galaxies and using spectroscopic observations of this host enables us to measure the cosmological redshift to infer their distances [35].

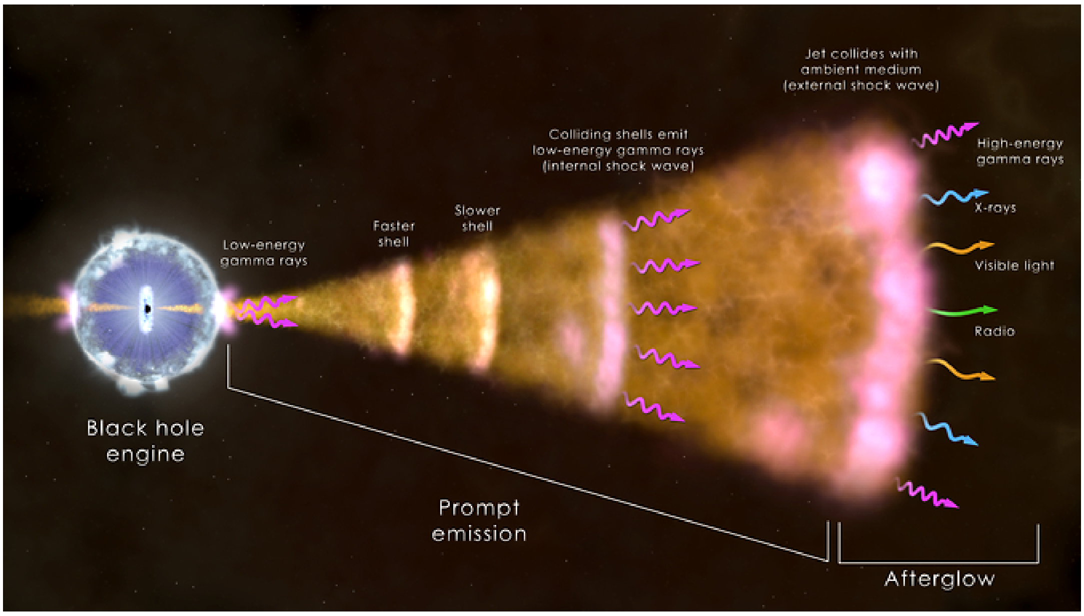

Figure 6: The fireball model, the prompt emission is explained by internal shocks within the jet. The afterglow is caused by the jet's interactions with the surrounding material [36].

Due to the high energies (up to about 10^{51} to 10^{52} erg after accounting for the beaming) involved in the ejecta and the short timescales of these variable systems, GRBs are likely related to black holes and/or neutron stars. These are compact enough to explain the enormous energy release over such a short timescale [37]. Aside from this, the rapid variability (i.e. $\delta T \sim 1\text{ms}$) of the observed lightcurves indicates that source is very compact since

$$R < c\delta T \sim 3000\text{km}, \tag{7}$$

where R is the size of the source [38]. However, due to relativistic effects, this limitation may be relaxed by a factor of γ^2 [22], where γ is the Lorentz factor of the shocked ejecta.

The extreme nature of the central engine of GRBs brings along observational and modelling difficulties as these objects are opaque to electromagnetic radiation. Aside from this, the observations of GRBs have shown great variability for each burst in a number of properties [39]. Despite these difficulties, a unified theory of GRBs is starting to take shape. In the following sections, an overview of the most commonly discussed models on formation and emission in GRB theory will be set forth.

2.1 The Physical System

From observations it has been noted that GRBs can be divided into two categories based on the time it takes to observe 90 % (from 5% to 95%) of the fluence of a GRB. This duration is called T_{90}. Long GRBs have a duration of more than two seconds while short GRBs last less than two seconds. An illustration of this observation can be seen in Fig. 7. The former variety constitutes the largest portion of all GRB observations and because of this, they have been studied in greater detail than their short counterparts [40].

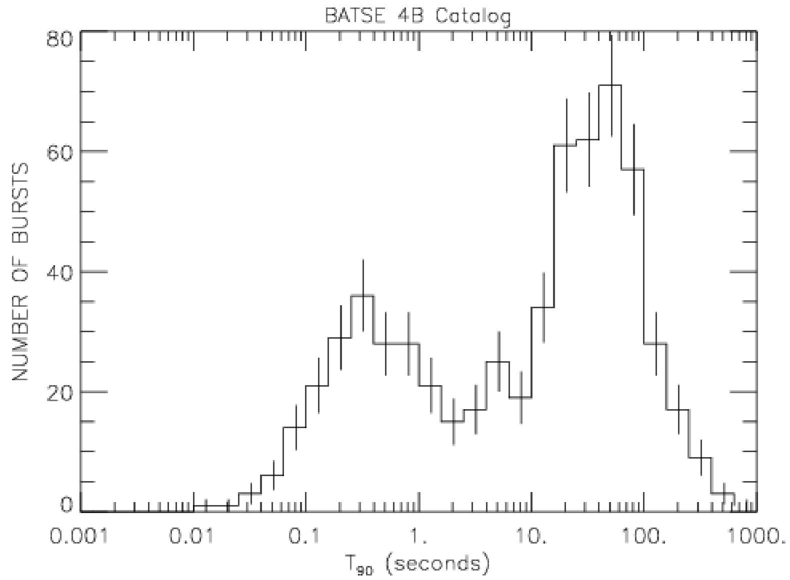

Figure 7: The distribution of T_{90} durations of GRBs indicating two distinct groups [41].

2.1.1 Progenitors

A large number of well-studied long gamma-ray bursts have been linked to core-collapse supernovae of Type Ic. Supernovae of type Ic result from massive stars which got rid of their outer hydrogen and helium layers due to either stellar winds or interactions in a binary system. These type of stars are named Wolf-Rayet stars [44]. They are located in galaxies with rapid star formation, which has been confirmed by long GRB afterglow studies. To sustain the release of energy it is supposed that the progenitors are Wolf-Rayet stars with an initial mass exceeding $\sim 40 M_{\odot}$ (with $M_{\odot}$ the mass of the sun). Although Wolf-Rayet stars can start with an initial mass of $20 M_{\odot}$, the larger mass is necessary to explain the large energy release of long GRBs [45].

The progenitors are suspected to be rapidly rotating and are possibly highly magnetized. These properties are assumed as they can prevent an instantaneous core collapse and lead to the sustainability of a jet. A sustained but variable energy release over a short time period is observed instead of a sudden instantaneous energy release. Due to this, the progenitors are most likely low in metalicity to allow for the large mass and rapid rotation. Stars with a high metallicity are observed to have high rates of mass-loss and would thus lose too much mass before a GRB would occur [45, 46].

Short GRBs have been observed to occur some distance away from their host galaxy. This indicates that they have received an initial kick due to a SN explosion which expelled them from their galactic environment. The large energetics involved in this process and the short timescales in which the phenomena occur leads to promising candidates of progenitors of short GRB sources such as binary neutron star (NS) mergers or neutron star-black hole (BH) mergers [40]. Recent observations claim to have detected a kilonova[3] infrared transient about 10 days after the burst from the short GRB 130603B. This is consistent with the binary merger models in which r-process nuclei[4] produced in the neutron-rich ejecta provide the infrared energy via their radioactive decays [48, 49].

A merger between a NS and NS or BH (GW170817) has also been inferred from observations of gravitational waves with LIGO (Laser Interferometer Gravitational-Wave Observatory) [6] together with a short GRB detected by Fermi [7]. Gravitational wave observations of GRBs will be one of the hottest research subjects in the next few years. The future correlation study between gravitational waves and neutrino detection will be of great importance in this field.

2.1.2 Central Engine

Both the collapsing star model and the merger model require the central engine to be a compact object. A compact engine would clarify the observed rapid variability in both long and short GRBs. A single catastrophic event, either being a merger or a star collapse, cannot explain the GRB lightcurve features. It is assumed that GRBs have a quasi-stable central engine [45, 50].

The most likely candidate for the central engine is a black hole powered by the accretion of matter in an accretion disc. A second possibility for the central engine would be a newly formed millisecond magnetar, which is a highly magnetized and rapidly rotating neutron star. The former candidate extracts gravitational energy from the accretion disk which gets converted into a jet. Whereas the latter, the millisecond magnetar, would be powered by the spin down of the object. The rotational energy loss of a magnetar due to this spin down is typically $\dot{E}_{rot} \sim 10^{50} - 10^{51}$ erg s^{-1}. A magnetar would eventually

[3]A kilonova is a transient phenomenon which has a peak brightness of 1000 times that of a generic supernova. It occurs due to a BNS merger or binary BH-NS merger [47].

[4]The r-process, or rapid neutron capture, is a process of nucleosynthesis where the heavy nuclei present in our Universe get formed due to the capturing of neutrons by these atomic nuclei. It is 'rapid' in the sense that the neutron capture rates are so high that the nuclei do not have time to β-decay before being hit by another neutron [48].

collapse as it spins down, as the hyper/supermassive object is no longer sustained by its rapid rotation and strong magnetic field [51].

The jet created by the accretion of matter by the black hole would be aligned with the rotation axis of the black hole and the original system. If the initial jet produced by the central engine is rather weak, a second more energetic jet could be formed by the fall back of material in the initial jet, which is accreted back onto the black hole. The nature of accretion (matter or magnetic flux accretion) is related to the nature of the jet as it influences the initial bulk Lorentz factor of the jet, the GRB duration and whether the jet is matter- of Poynting flux-dominated [52].

For a short GRB, the central engine is dependent on the original constituents of the progenitor system. If before the merger we have a black hole, the central engine will be a black hole. However, if the progenitor is a neutron star binary, then the central engine might be a hypermassive magnetar depending on the original masses of the constituents and the equations of state. For long GRBs, either a black hole or a magnetar could theoretically function as the central engine [45].

2.2 Prompt Emission

The prompt emission mechanism depends strongly on the energy distribution between matter and magnetic fields in the established jet. Particles are accelerated by some mechanisms (e.g. shock acceleration) in the jet and will thus emit photons which are observed as prompt emission. If the baryonic matter carries the bulk of the energy in the jet, the main mechanism of acceleration is explained by the fireball model [53]. On the other hand, if the bulk of the energy is carried by the magnetic fields, then the acceleration mechanism is believed to be explained by the magnetic field-dominated jet model [59].

In the fireball model, where most of the energy is contained in the matter constituents, the jet is mainly made out of radiation and electron-positron pairs. The 'fireball' in the model's name refers to the fact that the total energy is much larger than the rest energy and thus that there is a high radiation density in the jet. The evolution of the jet is strongly influenced by the number of baryons. High amounts of baryonic matter will cause a large portion of the available energy to be converted to the kinetic energy of the baryons. However, if the amount of baryonic matter is too high, the jet would be unable to achieve the high Lorentz factors which are required based on observations. A jet is thus high in energy density but relatively low in matter density [54].

The initially optically thick jet will propagate outwards and cools down along its propagation. Photons created in the jets high-density environment interact with each other to create electron-positron pairs. During this cool down process, the density decreases such that photons created in the jet can escape, i.e. the jet becomes transparent. The transition surface where this transparency occurs is called the photosphere. This released radiation might manifest itself as a precursor or might contribute to the prompt emission of the GRB [55].

The jet is not expected to be homogeneous, as the central engine will emit matter and radiation in an irregular stream. Areas, or shells, of variable density, will be emitted with different Lorentz factors. When a faster shell catches up with a slow one, a high-density region forms and a strong local magnetic field exists, since the magnetic field lines becoming extremely condensed in this area. This interaction between the shells is in the form of an internal shock. These magnetic inhomogeneities are the main components for another phenomenon, namely first-order Fermi acceleration [56]. When a charged particle, e.g. an electron, travels through this magnetic inhomogeneity, it gets scattered and gains energy by this interaction. When the charged particle crosses multiple times, it will get boosted each time [57].

Despite the particle's gained energy with each crossing of the shock, other phenomena cause the particle to lose energy (e.g. inverse Compton scattering and synchrotron radiation). It is thus not possible to accelerate the charged particle to arbitrarily high energies. The magnetic inhomogenous field lines causing the acceleration might cause a loss of energy through synchrotron emission when the particle spirals around the field line. Photons will be emitted due to radial acceleration [58].

The second model, the Poynting flux-dominated jet model, does not rely on local (i.e. much smaller than the jet dimensions) magnetic field inhomogeneities, but rather on the global and large scale magnetic field of the system. In this model, it is assumed that the bulk of the energy is propagated by the Poynting flux rather than the kinetic energy of particles. When the magnetic field lines of the system split and reconnect, they release energy in the surrounding plasma, which causes charged particles to be accelerated indirectly [59].

For both models, the resulting emission consists of hard x-ray and low energy γ-ray synchrotron photons, accelerated electrons and possibly hadrons if the jet is dense enough. However, due to the presence of a strong magnetic field in the Poynting dominated model, the radiation will be polarized in contrast to the fireball model. Low energy photons can get scattered on high-energy electrons, transmitting their kinetic energy to the photon, resulting in high-energy γ-ray photons. This phenomenon is called inverse Compton scattering. Both electrons and hadrons can be accelerated by the mechanisms described earlier. A proton-photon interaction can create an electromagnetic cascade which produces high-energy photons and possibly neutrinos [53, 59].

There are two main processes which can produce high-energy neutrinos. The pγ-interaction is a standard process which can take place in the jet of a GRB. Additionally pN-interactions can happen if the jet interacts with nearby matter [60]. The following interaction might occur in the jet of a GRB,

$$p + \gamma \rightarrow \Delta^+ \rightarrow \pi^+ + n, \tag{8}$$

in case of a high abundance of photons. This hadronic interaction will only occur if the energy of our proton and photon exceed the Δ production threshold

$$E_p E_\gamma > \frac{m_\Delta^2 - m_p^2}{4}. \tag{9}$$

For instance, a highly relativistic proton from the jet with an energy of $\sim 10^{16}$ eV interacting with a UV photon of about 10 eV. This high-energy photon might originate from synchrotron radiation in the jet. It may be boosted by Inverse Compton (IC) scattering by the highly relativistic electrons as mentioned earlier. The produced Δ will decay into a pion and neutron and the pion itself will decay into a muon neutrino and an anti-muon [26],

$$\pi^+ \rightarrow \mu^+ + \nu_\mu. \tag{10}$$

The energy gets distributed unevenly among the produced particles. The produced pion has about 20% of the energy of the primary proton and in the pion decay, the muon neutrino receives only about 20% of the energy of the pion. As a result, the produced neutrino has only 4% of the energy of the primary proton. However, as the proton is a highly relativistic particle, this might still result in a high-energy neutrino ($\sim$2 orders of magnitude lower in energy than the primary proton) [22, 26]. The 10^{16} eV proton mentioned before would thus produce a 400 TeV muon neutrino.

If there is matter surrounding the GRB, the relativistic protons in the jet might interact with the nucleons in the surroundings. This will give rise to pN-interactions

$$p + N \rightarrow pions + X, \tag{11}$$

where N is a nucleon and X can be a combination of different particles. The produced pions can have one of three charges, π^+ π^0 and π^-. The π^+ decay as in Eq. 10. If the produced pion is a π^- it will decay as,

$$\pi^- \rightarrow \mu^- + \bar{\nu}_\mu. \tag{12}$$

For the π^0 we have

$$\pi^0 \rightarrow \gamma\gamma. \tag{13}$$

These photons will mainly convert to electron-positron pairs or lose energy by Compton scattering. This prohibits us to uniquely identify the photons from π^0 decay [26].

2.3 Afterglow Emission

As the jet propagates outwards, it encounters material that surrounds the progenitor system. This material might have been ejected in an earlier phase or might be a part of the surrounding interstellar medium. The energy of the shock wave is concentrated in the jet head and when this shock collides with the surrounding medium it launches two shocks. A forward shock downstream the jet's head and a reverse shock towards the progenitor. The reverse shock is still travelling forward but is slower than the jet itself, therefore apparently moving in reverse [61].

The afterglow's main emission mechanism is synchrotron radiation. Modelling of the broadband afterglow emission for radio to x-ray observations agrees with this assumption. As the jet's head slows down, the reverse shock catches up. When the reverse shock crosses the bulk of the jet's material, the electrons get excited and emit a single flash of photons when they turn back to their lower energy states. The emitted radiation is observed to have optical or longer wavelengths. This energetically lower radiation from the reverse shock is due to the relative weakness of this shock (compared to the higher energetic internal or forward shock)[61].

The forward shock at the head of the jet produces synchrotron radiation in the higher end of the spectrum (high-energy γ-rays, up to several 100 GeV). As the shock slows down, the synchrotron emission becomes less energetic as time progresses. The forward shock component of the afterglow is emitted in successively lower energy bands. The different components of the afterglow combine in our observations as the emission from the forward shock might be starting while the jets internals are still releasing prompt emission [61].

3 Precursors

Precursors were discovered shortly after the initial observation of GRBs. A detailed study of a gamma-ray burst in 1974, using observations made by the γ-ray and x-ray spectrometers aboard the Apollo 16 mission, has provided the first detailed light curve, energy spectrum observations (between 2.0 to 7.9 KeV and 0.067 to 5.1 MeV) and source location of a GRB. The lightcurve of this GRB can be seen in Fig. 8.

This study reported a dim but well-defined peak in brightness before the dominating emission (i.e. the prompt emission), that was regarded as a probable precursor. This probable precursor was defined as a period of emission which had an observed photon rate 3σ above the background, but was much dimmer than the prompt emission. The study indicated that the precursor was most likely initiated by a different mechanism than the prompt emission. This was found when examining the hardness ratio, being the ratio between the photon count above and below a fixed energy, of the γ-ray emission. The prompt emission was observed to have a softer variable component alongside a hard component whereas the probable precursor only was observed to have a hard component. The observation that the beginning of the emission was not dominated by the most explosive phase (resulting in a bright start) was an interesting discovery as naturally one would expect that the beginning of the event would be dominated by the larger energy releases as is common in explosive phenomena [72].

As seen earlier, GRB gamma emission observations discredit the assumption that these events are simple violent bursts of high-energy electromagnetic emission. The observed emission is highly variable, which is predicted in various GRB jet models. These models allow for complicated interactions, which in the fireball model take place in the high energy density regions that form when a fast shock wave collides with an earlier slower one in the jet. Precursors could potentially be due to a part of this mechanism in cases where Lorentz factors of subsequent shells are similar. Another possibility, in which the precursor emission is originating from the same physical origin as the prompt emission, could be a mechanism in which the prompt and precursor emission are separated in time due to a temporary shut off of the central engine. To date, the physics behind such a potential central engine shut off remain unclear. It is, however, a possibility that is considered. A broad variety of mechanisms unrelated to the emission produced in the prompt emission phase could be responsible for the emission in the precursor [45]. An overview of potential precursor mechanisms will be given in section 3.1.

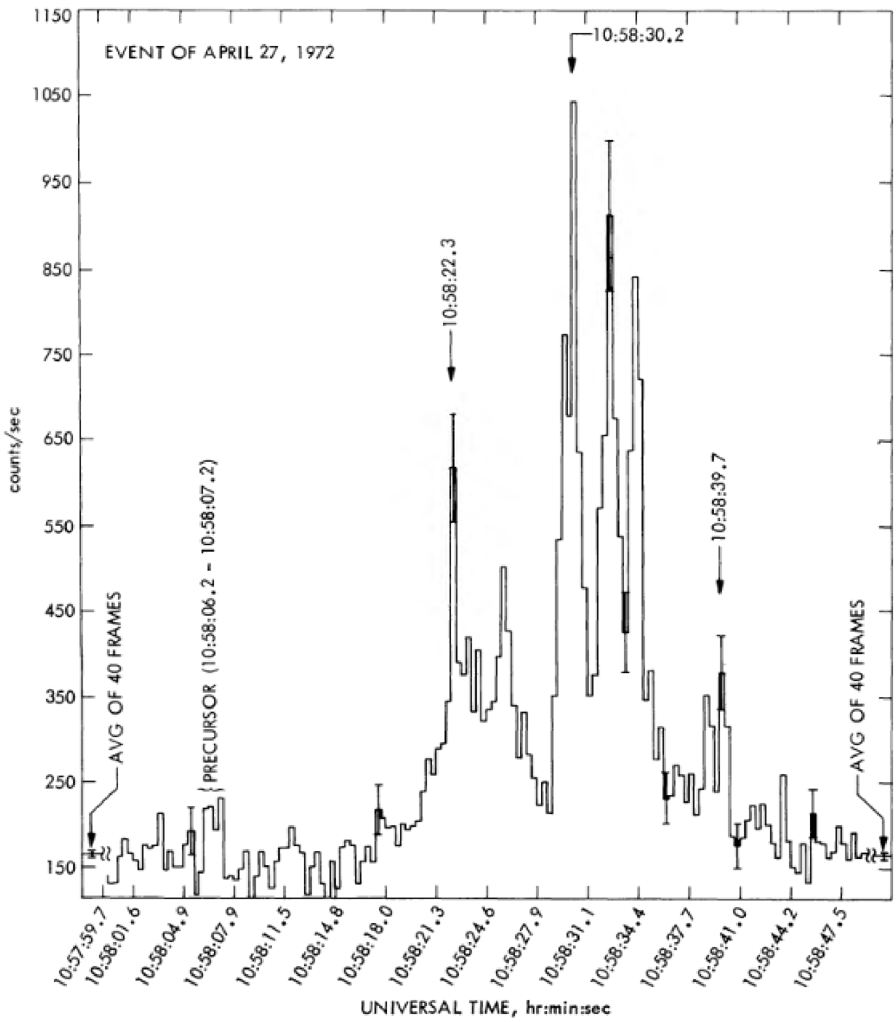

Figure 8: The lightcurve of GRB 720427, indicating the precursor in the time interval (10:58:06.2, 10:58:07.2), as observed by the instruments aboard Apollo 16 [72].

GRB population studies have been conducted to quantify and understand the precursor and prompt emission properties. This in order to identify whether the prompt emission properties depend on the precursor properties or to uncover whether the prompt and precursor emission are inherently different. A brief overview of some of the most prominent studies will be given in section 3.2. From these population studies, it has been observed that precursors occur in less than 20 % of the observed GRBs. The exact amount, however, differs from study to study as the identification of a precursor depends strongly on the instrument used for the study, how a precursor is defined (as the exact definition may vary among studies) and the methodology applied to find them. The definition for precursors used in this thesis and the methodology applied to identify them will be clarified in section 4.

3.1 Precursor Mechanisms

A variety of models have been developed to describe the precursor emission mechanism in the assumption that precursors are caused by a different mechanism than the prompt emission. If the precursor emission site is located near the emission site of the prompt emission, the quiescent period would be relatively short as both regions would be energized subsequently by the energy outflow. In this section, a brief overview of the most prominent models will be given, starting with models where the prompt emission site is located near the one of the prompt emission and thus have a short quiescent period.

3.1.1 Photospheric Precursors

In this model, the emission observed during the prompt phase originates from an initial optically thick jet. The thermal radiation produced in the jet cannot travel very far without interacting with the jet's medium as the mean free path of the photons is much shorter than the jet's dimensions. Therefore, photons cannot easily escape the jet. As the jet propagates outwards it expands, becomes less dense and the mean free path of photons increases. When the jet becomes optically thin, photons are able to escape the jet's confinement. The photospheric emission thus will occur during this transition period. However, it is still debated whether it could be bright enough to be observed as a separate component alongside the prompt emission [62].

If the precursor mechanism is due to this photospheric emission and if it occurs separated in time from the prompt emission, the precursor would have a thermal or quasi-thermal spectrum peaking in x-rays. In contrast, the prompt emission has a non-thermal spectrum predominantly in γ-rays. The prompt emission, if caused by internal shocks at approx. 10^{13} cm from the central engine, would occur several milliseconds to a second after the precursor emission [62, 63].

In the case of a magnetically dominated jet, a longer quiescent period is possible as the prompt emission site, energized by the reconnection of magnetic field lines, is further away from the central engine (approx. 10^{16}cm). The photospheric emission in this case, however, is assumed to be very dim. This is due to the jet's energy not being stored in an expanding fireball, but rather in the magnetic fields which do not contribute to thermal radiation [63, 64].

3.1.2 Shock Breakout Precursors

Long GRB progenitors are assumed to be massive stars which have undergone a core collapse. A stellar envelope comprised of the outer layers of the massive stars surrounds the central engine. When a jet is emitted by the central engine, it collides with the stellar envelope and heats up the material causing it to radiate thermal photons. When the jet manages to break through the material, the thermal radiation releases in the form of a shock breakout about one to 10 seconds before the prompt emission [65].

As the produced thermal emission is not strongly beamed and the jet's energy is distributed over a large surface of the stellar envelope, it is likely to be very dim and hard to observe. Highly energetic particles in the jet are able to interact by inverse Compton scattering with photons from the shock breakout to produce a second (non-thermal) precursor containing high-energy gamma radiation approximately a second before the prompt phase. Due to the similar properties as the prompt emission, this phenomenon is hard to tell apart from the prompt emission [65].

The shock breakout emission mechanism may also occur in short GRBs, although it is less likely compared to long GRBs. If the progenitor of a short GRB, e.g. a binary neutron star merger, produces a dense baryon-loaded wind with which a jet can interact, a shock breakout might occur [66].

3.1.3 Fallback Precursors

The fallback mechanism is similar to the shock breakout mechanism as it relies on a medium closely surrounding the central engine, which interacts with a jet. The mechanism is thus more likely to occur in long GRBs as these have a stellar envelope surrounding the central engine. In this mechanism, a weak jet is emitted by the central engine which can not penetrate the stellar envelope completely. The mechanism emitting the jet slows down and the material that interacted with the jet collapses onto the central engine which powers a second stronger jet which does break through the surrounding medium [67].

The first weak jet would produce non-thermal emission, similar to the emission from the stronger second jet. The quiescent period between the precursor and prompt emission would be determined by the time it would take for the material, which interacted with the first weak jet, to fall back onto the central engine. This time interval is estimated to be about 100 s [67].

3.1.4 Multistage Collapse Precursors

In the case of a rapidly rotating progenitor, a temporarily stable system, called a spinar, might occur before collapsing into a black hole. In such a system, the centrifugal and gravitational forces balance each other such that a stable phase is possible [68].

The parameters in the models describing general spinar phenomenology allow for potential bursts (similar to what has been observed in precursors) with a large variation in intensity and quiescent period durations. The model predicts that approximately 10% of GRBs have a quiescent period of more than 100 s. An in-depth explanation of this model can be found in [68] and [70].

3.1.5 Neutron Star Crust Cracking

If the short binary merger scenario for short GRBs involves at least one neutron star, the crust of the neutron star will be affected by tidal forces before merging. Due to these strong tidal forces, it is possible that the crust will crack and release large amounts of energy. To date, it is unclear whether this phenomenon could release enough energy in the form of electromagnetic radiation to be able to observe [70].

The release of energy due to a crack would occur shortly (milliseconds) before merging [70]. It could potentially occur due to the manifestation of a resonant effect caused by the rotating binary, which would be several seconds before the merging of the binary. This would allow for longer quiescent periods [71].

3.2 Population Studies

Since the first observation of a GRB and the discovery of precursors, various population studies have been conducted on data from different observatories. Each study has its own definition of a precursor and method of detecting them. This makes it difficult to directly compare or combine studies in order to generate conclusions. However, even despite the inconsistency between studies, a general consensus of precursor and prompt emission properties is starting to form. A standard definition for a precursor would, for instance, be the demand for the precursor emission period to be dimmer than the prompt emission. A second criterion is that the precursor precedes the dominant emission by a quiescent period (a time interval in which the background subtracted light curve is approximately zero). This definition allows for a certain degree of flexibility, as for example, the exact length of the quiescent period is not defined.

An early study conducted in 1995 conducted by Koshut T.M. et al. examined 1000 BATSE GRBs [73]. They have found precursors in 3% of the total sample. However, in this study, strict constraints regarding the duration of the quiescent period were imposed. The duration of the quiescent period was required to be larger than the duration of the prompt emission. The selection of precursors from the sample was done by eye. To define the duration of emission periods a signal-to-noise ratio was used and to study the spectral properties of the prompt and precursor phase the hardness ratio was examined. The research concluded that there was no significant difference in temporal properties between the emission during the prompt and precursor emission periods. The properties of the prompt emission do not seem to be influenced by the properties of the precursor [73].

The study conducted by Burlon D. et al. in 2009 on 2121 GRBs observed by BATSE has found that 12.6% of these contain precursors [74]. The definition of a precursor in this study was defined as an emission period with a peak flux which is smaller than the peak flux of the prompt emission which follows it. The precursor phase and prompt emission phase are required to be separated by a quiescent period as described by the standard precursor definition. The precursor selection method is not explicitly mentioned in their paper, presumably, it is done by eye. In order to characterize temporal periods (e.g. the time interval of the precursor) they used T_{90} measurements. The study concluded that precursors are indistinguishable from the prompt emission as they display similar spectral properties and have similar trends in spectral evolution, independent of the duration of the quiescent period [74].

In another study conducted in 2014 by Charisi M. et al., long GRBs recorded by BATSE, Swift (BAT) and Fermi (GBM) [75] were investigated. In total, the sample contained 2710 GRBs. The standard definition of precursors was applied in this paper and about 10% of the sample was found to contain a precursor, this number has been verified by separate analyses from multiple instruments in the study. No correlations in temporal properties were found between the precursor and prompt phase. There was no analysis of spectral properties in this study [75].

A recent study of GRBs was conducted by Zhu S [45]. in 2015. In this study, the sample consists of 1275 GRBs observed by the Fermi GBM up until the end of 2013. The lightcurve is created by binning the TTE and CTIME data by applying a specific binning algorithm, namely the Bayesian block algorithm. The standard definition of precursors was adapted into three different precursor types. A first type is much dimmer (approx. one-third dimmer) than the prompt emission and has a well defined quiescent period. A second type is also much dimmer than the prompt emission (similar to type one), however, there is no constraint demanding a quiescent period. At last, for the third type, the constraint demanding a dimmer precursor was loosened, no longer requiring it to be three times as dim as the prompt emission. A quiescent period is not required for this type. The selection of precursors was done by eye. From the sample, about 16% of GRBs contained a precursor of one of these types. After detailed studies for each of these types, no exclusive distinction between precursor properties and prompt emission properties was found. It has been noted that the observed long quiescent periods in GRBs with a prompt emission duration much smaller than 100s are hard to explain with the standard jet models available [45].

These studies seem to indicate that there is no correlation between precursor and prompt temporal properties. This thesis will follow loosely the methodology to create lightcurves set forth by Zhu S. by using the Bayesian block algorithm, this in order to complete a precursor sample from all available data available by Fermi GBM (up until 2019). In order to evaluate and select GRBs with precursors from a sample containing all observed GRBs by Fermi, an automated selection method will be devised.

4 Identification of the GRB Precursor Phase

The aim of this study is to find a temporal window in which the precursor phase of GRBs is located. During the precursor phase of GRBs, the dense environment is expected to cause an increased neutrino production. As such, this window would be of interest for the detection of GRB neutrinos by the IceCube Neutrino Observatory.

To obtain this temporal window, CTIME and TTE data from GRB detections from the Gamma-ray Burst Monitor from the last eight years (2011 until 2019) will be examined. This period is chosen because it coincides with the data taking period of the completed IceCube observatory. The data from all GBM instruments are used. However, for each observed GRB only the instruments with the smallest viewing angles to the burst location are used in this study. If three or more detectors are triggered, three signals will be examined. Whereas, if two detectors are triggered, only two signals will be examined. The constructed set of data contains measurements of 1545 long GRBs ($T_{90} > 2$s) and 309 short GRBs ($T_{90} < 2$s). As each GRB is observed by multiple instruments of the GBM, the data set contains 3393 long GRB trigger observations and 718 short GRB trigger observations. The features observed in each GRB trigger will be examined independently. To account for potential background fluctuations in the observed signals, the final precursor sample will only contain precursors that were observed independently by at least two instruments.

As discussed before, long and short GRBs are believed to have different progenitors as they display significant differences in their properties. Therefore, in this study, long GRBs and short GRBs will each be examined separately with the goal of identifying precursor GRBs (which will be a small subset of the total observed GRBs). This subset of precursor GRBs can then be used to characterize the temporal precursor window.

4.1 Precursor Definition

As has been seen in section 3.2, there is a high variability among studies regarding an exact precursor definition. In this thesis, the following definition of a precursor will be applied. It will be demanded for the precursor emission to be dimmer than the prompt emission and the precursor should precede the dominant prompt emission by a quiescent period (a time interval in which the background subtracted light curve is approximately zero). The precursor selection procedure is outlined in the following paragraphs and will be described in more detail in the next sections.

A first step towards obtaining our precursor GRB subset would be to identify the individual emission periods in each GRB. An emission period of a GRB is identified as a period in which the integrated photon count is at least 3σ above the integrated photon count of the modelled photon background rate for this period. The emission periods within a GRB are separated by quiescent periods, these are defined as periods in which the integrated photon count agrees with the integrated photon count of the background model for this period within 3σ. For each emission period, we determine T^i_{100} (i.e. the time it takes to observe 100% of the fluence of the i-th emission period) and for each quiescent periods T^j_Q (i.e. the duration of the j-th quiescent period) within the total GRB emission period T^{tot}_{100}. Here, T^{tot}_{100} indicates the period between the start of the GRB (i.e. the start of the first emission period) and the end of the GRB (i.e. the end of the last emission period). A visualization of T^i_{100} and T^j_Q can be seen Fig. 9. This figure contains the signal of a fictional GRB with three emission periods. The first emission period (at t = -150 s) is a probable precursor, i.e. an emission period which is potentially our precursor. The following two emission periods in this figure are the probable prompt, i.e. a collection of emission periods which is likely to be the prompt emission of the GRB. If the probable precursor is found to not be a precursor by the criteria applied in this thesis, it is identified as the first emission period of the prompt emission. If this is the case, the prompt emission thus contains all observed emission periods.

To achieve the identification of the individual emission periods, one has to determine the background rate over the whole period of the GRB. This is done using the CTIME data as described in section 4.3. To identify the bounds on periods which potentially have an increased photon count (and are thus part of an emission period), a Bayesian block analysis [82] will be applied on the combined TTE and CTIME data as explained in section 4.2.

Secondly, it is not always clear whether two subsequent individual emission periods within an observed GRB signal are truly independent (e.g. they might only be separated in time by several milliseconds). The emission within a single emission period can be extremely variable. It is thus reasonable to assume that, if the quiescent period between emission periods is smaller than a certain time interval, this emission is not independent. If this is the case, the two emission periods are then classified as a single emission period in this study. To achieve this lower limit for the quiescent period, the variability in the photon count rate within the emission periods for all long and short GRBs will be examined. More specifically, the time interval between peaks in the observed photon rate for each individual emission period will be determined as this will uncover the details about the emission variability of GRBs. The k-th time interval between the maximum peak rates of the emission periods for all GRBs is indicated by T^k_P. This time interval is indicated in Fig. 9.

When there is more than one emission period in a GRB and the quiescent period between two subsequent individual emission periods in this GRB is relatively small in comparison to an upper limit of the earlier determined time intervals T^k_P for all GRBs, then these two emission periods will be regarded as a single emission period in this GRB. This reduction of the number of individual emission periods will be applied to the whole set of observed GRBs. It will act as the first criterion via which precursors will be selected, namely the quiescent period between two emission periods (presumably the precursor phase and the prompt phase) will be compared to the characteristic period between peak rates in emission periods. If the quiescent period in between is too small, they will be regarded as a single emission period GRB and will no longer be considered as a possible precursor GRB. This analysis will be conducted separately for long and short GRBs.

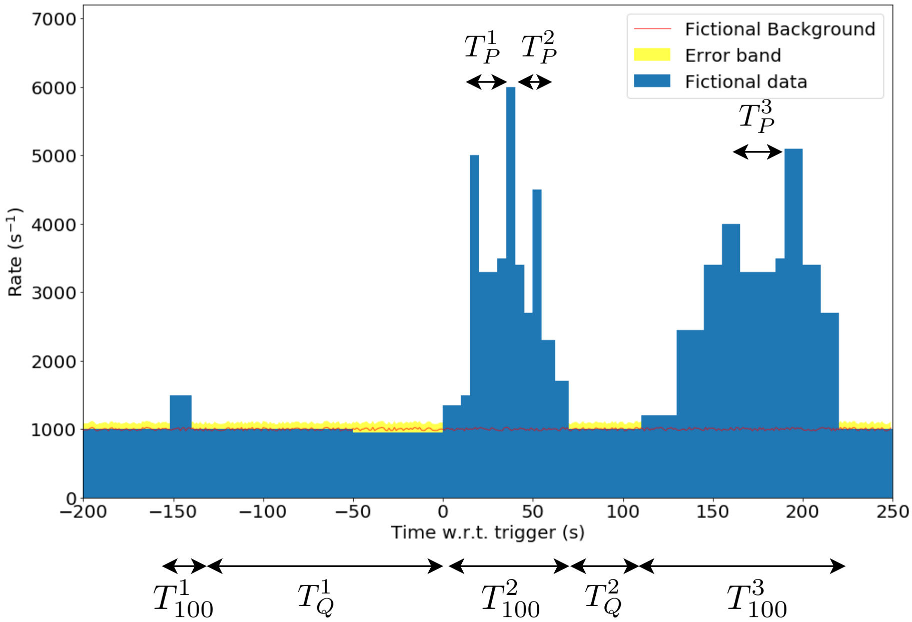

Figure 9: A fictional GRB with a precursor and two prompt emission periods to illustrate the various time intervals. In this figure we have indicated the following time intervals: the quiescent period between the precursor and prompt emission T_Q^1, the quiescent period between the prompt emission periods T_Q^2, the total emission period of the precursor T_{100}^1, the total emission period of the first and second prompt emission periods T_{100}^2 and T_{100}^3, the time intervals between the maximum peak rates in each emission period T_P^1, T_P^2 and T_P^3. In the first prompt emission period, there are three peak rates observed and there are thus two time intervals between the maximum peak rates.

The second criterion to identify precursor GRBs is that the photon count during the precursor phase should be significantly lower than the photon count in the prompt phase as precursors are relatively dim compared to the prompt emission. To account for background fluctuations there is an extra step to confirm the presence of a precursor in a GRB. A precursor is only validated if it is observed by at least two instruments from the GBM.

The resulting precursor sample will thus contain bursts which are relatively dim w.r.t. the prompt emission and have a well defined quiescent period. This definition excludes precursors with an extremely short quiescent period such as for example precursors emitted in the case of an expanding fireball model for the photospheric precursor mechanism or the non-resonant neutron star crust cracking mechanism. However, our sample is representative of other models which do predict longer quiescent periods. The main aim for the relatively broad definition in this thesis is to examine and quantify the temporal properties of a large set of precursors for subsequent GRB neutrino studies with the IceCube Neutrino Observatory, rather than examining the likeliness of a possible precursor mechanism.

4.2 Bayesian Block Algorithm

The binning of a histogram is often chosen in an ad-hoc manner by selecting a range and bin width with the aim of obtaining a subjectively good looking plot [76]. There are more objective methods available where the binning is optimized by a specific procedure. An example thereof would be Scott's Rule, where the number of bins with fixed width is determined by the number of data points and the root-mean-square as a measure of the spread of the distribution [77]. There are other procedures available (e.g. Freedman-Diaconis Rule and Knuth's Rule) which, as well, result in an optimized fixed width binning [78, 79].

The Bayesian block algorithm is different from this as it allows the binning to have a variable width for each bin. This procedure is developed specifically for the field of astronomy and is an objective way of quantifying abrupt changes in time series. Therefore, it is ideal for the study of GRB lightcurves and to serve as an online trigger algorithm [80]. See Fig. 10 for a comparison of Knuth's Rule and the Bayesian block algorithm for the binning of a histogram. The research conducted in this thesis makes use of the Bayesian block algorithm to construct the lightcurves that will serve as a basis for the GRB emission period analysis.

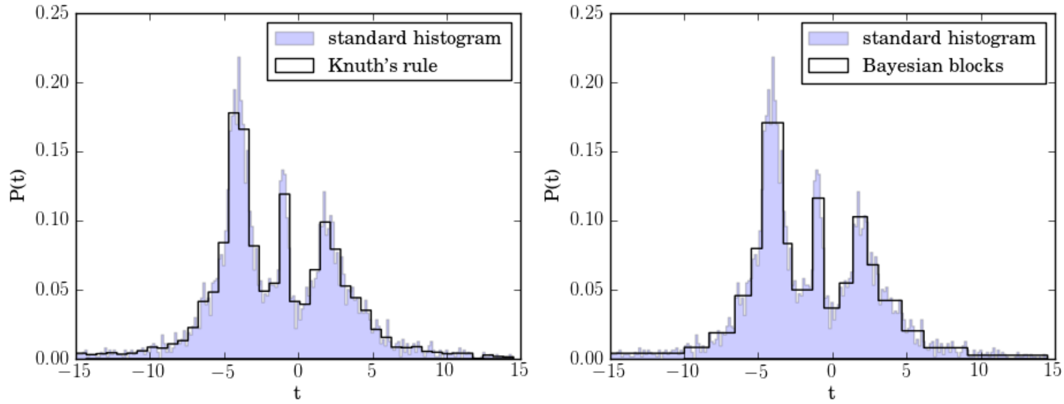

Figure 10: Two histograms displaying different methods on binning data (Knuth's Rule on the left, Bayesian block on the right) using a randomly generated dataset compared to a constant width binned histogram [81].

The Bayesian block algorithm is an unsupervised machine learning method for binning time series in histograms by detecting and characterizing structures localized in time in a non-parametric way. Localized implies that one searches for features in the time series in subranges of the total observational interval instead of looking for features spanning over the global interval. An example of such a global feature would be e.g. a periodicity, which is best analyzed by other means such as for example a Fourier or wavelet analysis. The algorithm is called a non-parametric method as it seeks for a general representation instead of fitting the data to a model [82].

The Bayesian block algorithm has been developed by Jeffrey D. Scargle to address the specific issue of the detection and characterization of local variability in time series in the field of astronomy. The goal is to allocate the edges of the bins, called change-points in this context, on moments in time when the flux from an observed astrophysical object undergoes a sudden change. The flux is defined by individual events, namely the arrival time of each photon in the detector. This event data (t_i for $i = 1, ..., N$) is used by the algorithm to determine the number of change points and their value [80].

The algorithm determines the number of blocks (or bins in a histogram context) and their edges by optimizing a fitness function (a goodness-of-fit statistic) which is dependent on the input data and a regularization parameter. It is set up in such a way that the constructed set of blocks will not be overlapping and no gaps will be present. The first and last data point will be respectively the beginning of the first block and the end of the last block. Each block can contain one to N data points and each data point only belongs to one block. The fitness of the blocks is cumulative, such that the fitness of a given set of blocks F_{total} is given by

$$F_{total} = \sum_{i=0}^{K} f(B_i), \tag{14}$$

where K is the total number of blocks and $f(B_i)$ is the fitness of the i-th block [80, 82].

The first step in the algorithm is to order all data points in time. From this ordered set of N data points, an optimized set of K blocks and thus $K+1$ change points will be determined by iterating through the data. With each iteration, the present maximum fitness values, as well as the reciprocal start and end indices, are saved. As the n-th data point is evaluated, the potential total fitnesses are determined by Eq. (14) as,

$$F_{total}(n, m) = F_m + f(B_m^n), \quad m = 1, 2, ..., n-1 \tag{15}$$

with F_m being the optimal fitness determined in iteration m and $f(B_m^n)$ being the fitness of the block between data point n and m. During this iteration, the potential total fitness is calculated $n-1$ times, the maximum fitness and its change points are stored and used in the next iteration. After the final iteration, the set of change points which resulted in the maximum total fitness is returned [80, 82].

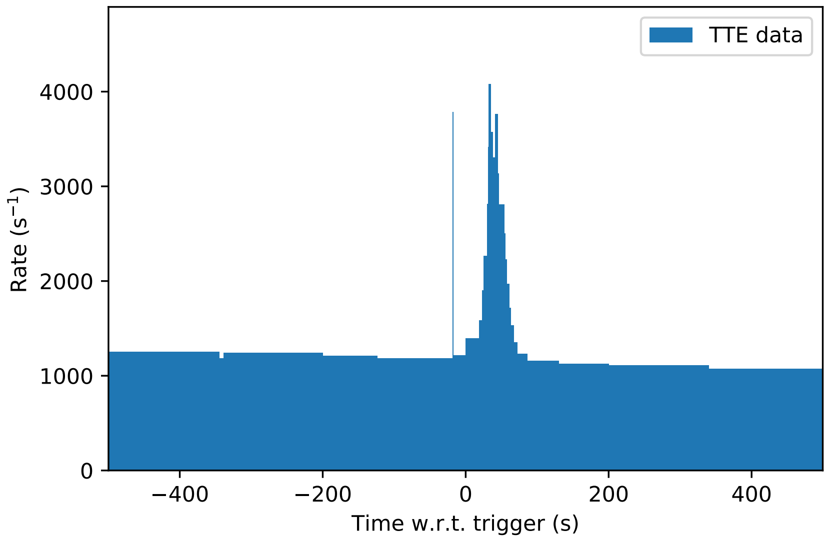

Figure 11: The Bayesian block algorithm applied on the combined TTE and CTIME data as detected by instrument n1 of the GBM for GRB trigger bn120204054. From this Bayesian block histogram it is noted that the GBM was not triggered by the precursor, but by the brighter prompt emission which closely follows it.

In this thesis the Bayesian block algorithm is applied to a combination of the observed CTIME and TTE data from the GBM. The high temporal resolution TTE data is provided in a limited time interval around the GRB trigger. To increase the time period in which we can detect emission periods, the TTE data is extended before and after the time interval in which TTE data is provided by the available CTIME data. The photon counts of each block (as determined by the Bayesian block algorithm) are divided by the time interval as defined by the change points of each block. The resulting rates for each block can be seen on the y-axis in Fig. 11. When referencing to the Bayesian block histogram later in this thesis, it is always implied that the photon counts as determined by the Bayesian block algorithm are divided by the respective time interval of the block.

4.3 Background

When a GRB is observed with one of the instruments of the GBM, there is always a γ-ray background noise present from other non-relevant sources. As in this study, the main focus is to observe and analyze GRB signals, it is necessary to isolate this noise from the relevant signal. To do this, multiple methodologies have been examined.

A first methodology that we developed is based on the assumption that the GRB prompt emission phase triggers the GBM instrument at t = 0s. As such the relevant GRB signal is assumed to be centred around this time. To characterize the background one could then select two intervals before and after the observed T_{100} of the GRB in the CTIME data and fit a polynomial through these data to represent the background during the whole observational period. The data used for this fit should not contain any GRB signals. This methodology is visualized in Fig. 12.

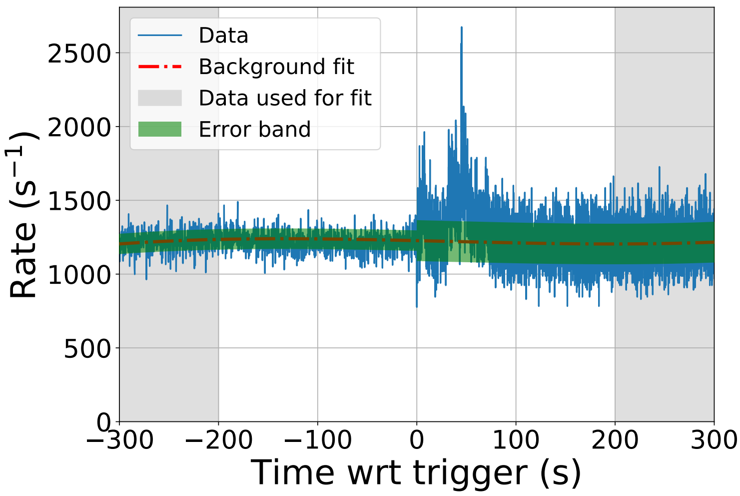

Figure 12: The background as detected by instrument n9 of the GBM for GRB trigger bn150105257. The data in this plot is comprised of CTIME data and the fit is a third order polynomial fitted through the CTIME data in the time intervals [-300s,-200s] and [200s,300s].

Despite the promising results for a large portion of the GRBs in the available sample, a smaller subset of the available data yielded sub-optimal background fits due to e.g. strong variability in the background rate. Therefore another methodology was devised.

The second methodology that is applied transforms the background by defining a running mean over the observed rates for all observed times. A linear fit containing the first 20 s of CTIME data is determined. This fit is used to predict the background rate 10 s after the fit region. It is checked whether the running mean agrees with the prediction of the fit. If the running mean of the observed rates does not agree with the prediction from the fit, then this time interval is likely to be part of a GRB emission period. Therefore the relevant rates in this time interval are discarded from the data set as they do not represent the background. This methodology is applied over the whole available CTIME data. The determined running mean will be used as our background rate in further analyses. The gaps in this data at times where former GRB signals were present are filled in with values resulting from interpolating the remaining (running mean) background rates at these specific times. The resulting rates are thus closely representing the actual background. An example of such a treated data set can be seen in Fig. 13.

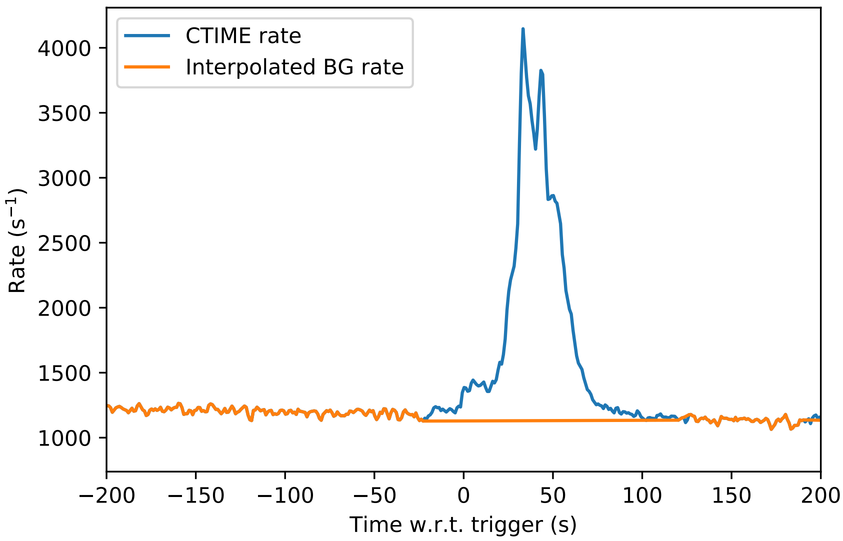

Figure 13: The background detected by instrument n0 of the GBM for GRB trigger bn120210650. The CTIME data has been smoothened by taking the average of the rate over intervals of one second to reduce the fluctuations when calculating the running mean. As can be seen from this graph, the background rate after the trigger at $t = 0$ is significantly less variable. This is due to the interpolation of the data which represents the background rate in this area.

The resulting interpolated background will serve as a close proxy of the real background for the detection of emission periods in GRBs throughout this thesis.

4.4 Emission Period Detection

After the quantification of a close proxy for the background rate using the CTIME data and the application of the Bayesian block algorithm on the TTE and CTIME data, one can start defining emission periods and quiescent periods in each GRB. The Bayesian block algorithm created change-points at times where the rate changes significantly from previous rates for each observed GRB.

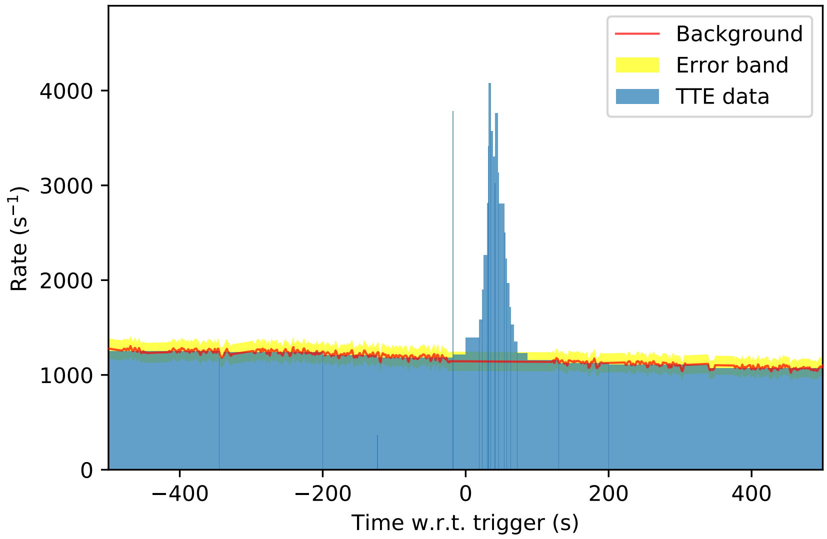

Figure 14: The Bayesian block algorithm applied to the TTE and CTIME data and the interpolated background from the CTIME data as detected by instrument n1 of the GBM for GRB trigger bn120204054. The error band is based on the Poissonian variation of the bin contents (i.e. $\sqrt{n}$).

To identify whether a block is part of an individual emission period in a GRB, the integrated photon count is calculated for this block and the corresponding background rates. The photon count for the block (n_{BB}) is calculated as

$$n_{BB} = r_{BB} \times \Delta T_{BB}, \tag{16}$$

where r_{BB} is the rate of the block and ΔT_{BB} is the time interval of the block between the change-points as determined by the Bayesian block algorithm. The photon count for the background n_{BG} is calculated by trapezoidal integration over ΔT_{BB} using the interpolated background rates defined earlier. As n_{BB} and n_{BG} are assumed to have a Poisson distribution, the accompanied errors ($\sigma_{n_{BB}}$ and $\sigma_{n_{BG}}$) are defined by the square root of the respective photon counts.

The block is flagged as part of an emission period in the GRB if the photon count of the background and the block differ by 3σ:

$$n_{BB} > n_{BG} + 3\sigma_{n_{BG}}. \tag{17}$$

Subsequent flagged blocks are recorded as one emission period. For each observed emission period, the individual rates and change-points for each block are recorded for later analyses.

This analysis is again conducted for both long and short GRBs. A database containing each GRB trigger is constructed from this analysis detailing the following properties: the number of emission periods, the rates in each emission periods and the times of the start and end of each emission period.

4.5 Peak Rate Criterion

To clearly identify two emission periods as two independent events, we examine the variability of the observed photon rate of each individual emission period for each long and short GRB in the respective dataset. Specifically, the period between peaks in the observed rate for each observed emission period of a GRB might disclose information about the variability of GRBs. If the quiescent period (i.e. the period between two subsequent emission periods in a GRB) is larger than e.g. an upper limit of the period between two subsequent peaks of observed rates from all emission periods in all GRBs, then one can say that these emission periods are not directly related. However, if they are smaller, these two subsequent individual emission periods could be regarded as one individual emission period. This criterion will remove GRBs from our sample in which the first emission period (a potential precursor) is likely to be part of the first prompt emission period.

The emission periods which are observed for each GRB in the previous sections can be used to provide statistics on the time intervals between peak rates (T_p^k for the k-th interval, this time interval is indicated on Fig. 9) within emission periods. In order to do this, the Bayesian block of each emission period for all GRBs have been examined for peaks or local maxima, where a local maximum is defined as any rate whose two direct neighbours have a smaller value. When two peaks are detected, the period between the end time of the first peak and the start time of the second peak is recorded. When more than two peaks are detected, the period between every two subsequent peaks is calculated as before and recorded.

An overview of the resulting values of time intervals between peak rates T_p for all emission periods in long and short GRBs can be found in Fig. 15. To distinguish two subsequent emission periods, we demand that the time interval between them has to be larger than at least the 90th percentile P_{90} of the distribution of time intervals between peaks. For long GRBs $P_{90} = 9.10$ s whereas for short GRBs $P_{90} = 8.27$ s. If for any of the GRBs the quiescent period in between two emission periods is smaller than this limit, it is (with approximately 90% probability) assumed to be a single emission period.

The result of this manipulation on the datasets for long and short GRBs can be seen in Fig. 16. As can be seen from the long GRB and short GRB barplots, the number of GRBs with two emission periods rises due to this manipulation. This, however, hides the fact that the reduction from two emission period GRBs to one emission period GRB has also taken place. The reduction from three or more to two emission period GRBs, however, outnumbers the reduction from two to one in this case. This manipulation is the first criterion on which precursors get selected, i.e. that the quiescent period between the precursor phase and the prompt emission needs to be larger than the value for the respective 90th percentile P_{90} for long and short GRBs. If, for example, a two emission period GRB has a quiescent period shorter than P_{90}, it will no longer be a precursor GRB candidate as it is from now on classified as a single emission period GRB.

4.6 Photon Count Criterion

In the first criterion based on the peak rates of emission periods, GRBs in which the potential precursor is merely a fluctuation of the first prompt emission period are filtered out. However, it still needs to be checked whether this first emission period is not just the first emission period of the prompt emission. Therefore, a second criterion is applied to select precursors. This criterion relies on the relative dimness of the precursor compared to the prompt emission. In cases where the first emission period is essentially the start of the prompt emission period, the emission period is assumed to have a brightness comparable to the prompt emission. However, if it is a precursor, it will be relatively dim compared to the prompt emission. This criterion effectively removes GRBs from our sample based on the brightness of this first emission period. In literature, a criterion is applied in the form of a hard upper limit on the peak flux ratio of the precursor emission and the prompt emission to select precursors [45].

A similar criterion will be applied in this thesis for the selection of precursors. However, instead of looking at the peak flux, the integrated (background subtracted) photon count will be determined for the T_{100} potential precursor emission period and the prompt emission period. If the photon count of the precursor is less than 15% of the photon count of the prompt emission it will be accepted as a precursor.

The "15% criterion" to select precursors is motivated by analyzing the distribution of the ratio r of the photon count of the probable precursor (i.e. the first observed emission period in a GRB) and the photon count of the probable prompt emission (i.e. the following emission periods). This distribution for long and short GRBs can be seen in Fig. 17. In the distribution for long GRBs, it is noted that for the photon count ratio being approx. 100 (2 on the $\log_{10}$ x-axis), the bimodal distribution has a local maximum. This implies that for the GRBs in this local maximum the probable precursor has a

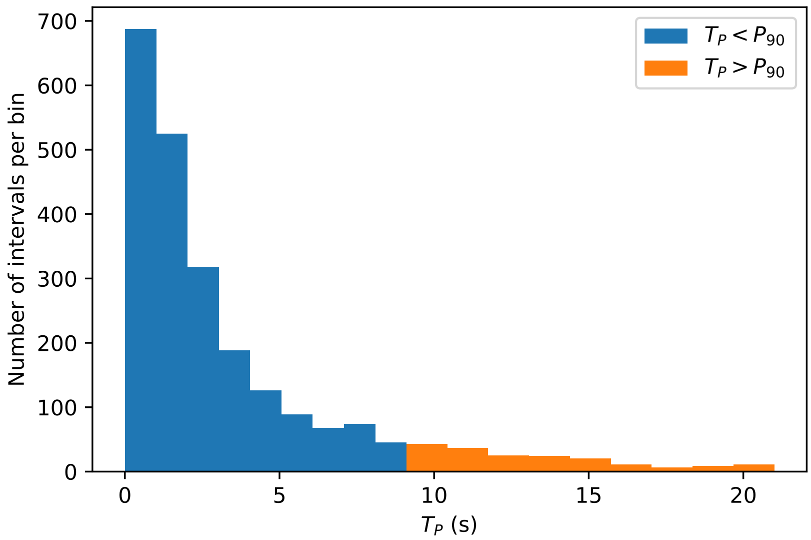

(a) Long GRBs, $P_{90} = 9.10$s

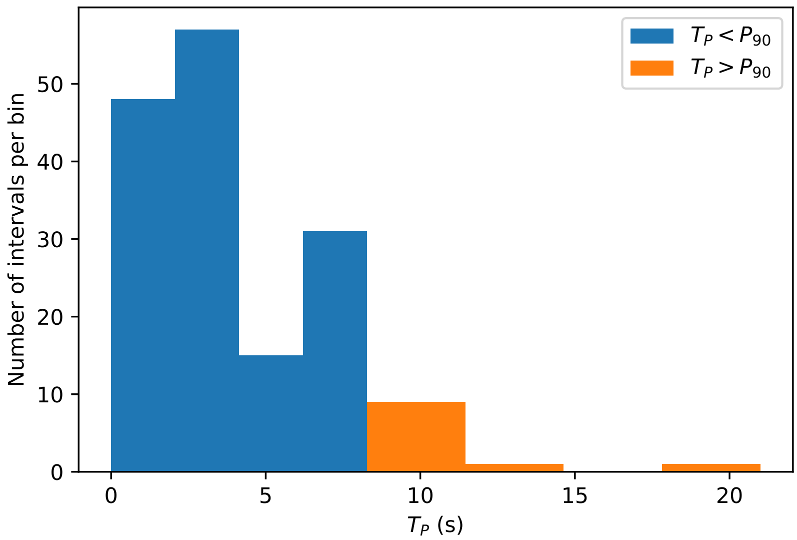

(b) Short GRBs, $P_{90} = 8.27$s

Figure 15: The distributions of the observed time intervals T_p between peaks in emission periods.

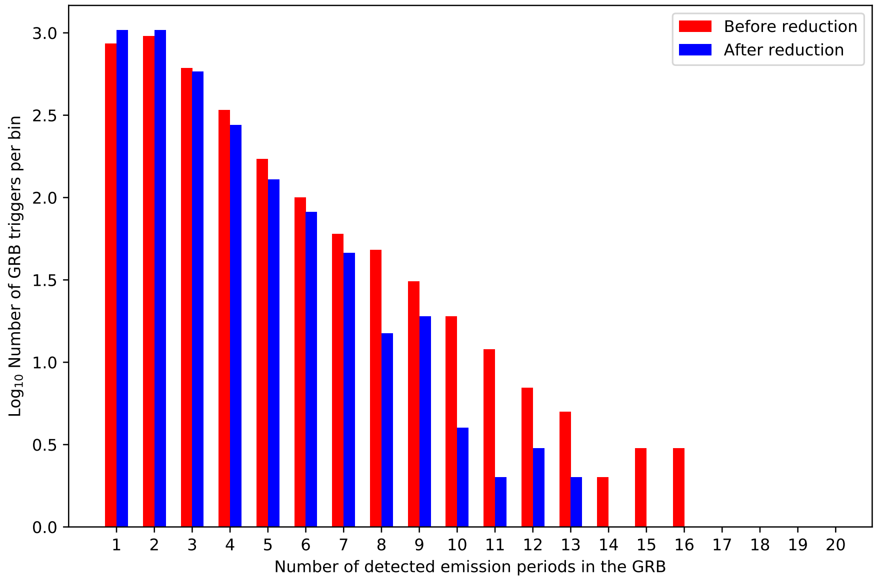

(a) Long GRBs

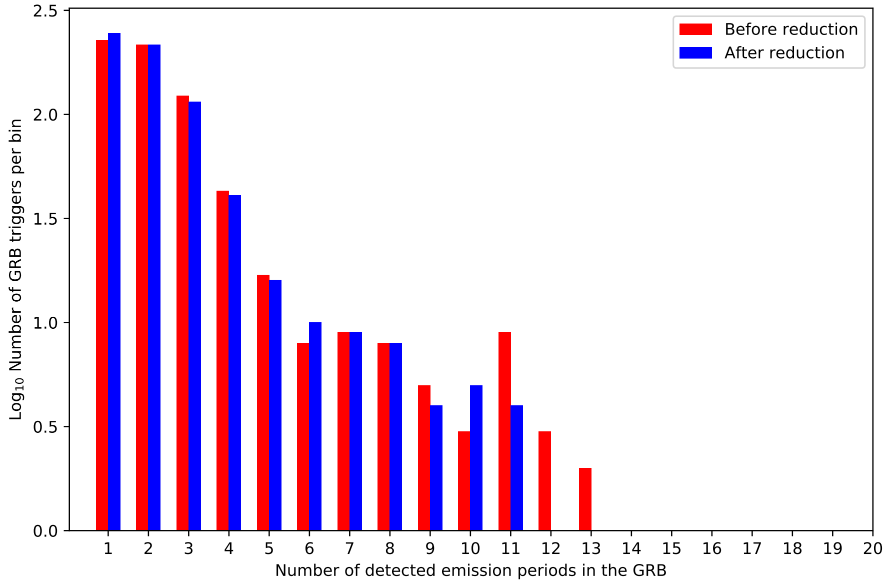

(b) Short GRBs

Figure 16: The observed long and short GRB trigger distributions by number of emission periods observed during the GRB before and after the reduction.

photon count of approximately 100 times the photon count of the probable prompt. The probable precursor is thus not likely to be a real precursor as it is very bright compared to the prompt emission. This probable precursor is thus identified as the first emission period of the prompt emission. A second local maximum is located at a ratio of 0.03 or 3% (-1.5 on the x-axis). Assuming that the precursor is dim compared to the prompt emission, this local maximum can be identified as GRBs in the distribution where the probable precursor is indeed a precursor. For a rate of 1 (0 on the x-axis), there is a local minimum. Here the photon count in the probable precursor and probable prompt is roughly equal. A similar analysis can be made for short GRBs. A lower limit of 0.15 or 15% on the ratio can be used to signify the end of the local maximum containing the precursor GRBs for both long and short GRBs.

GRBs in which multiple emission periods are present in the probable prompt phase are likely to have a higher photon count for the probable prompt than a single prompt emission period. This was considered to be an alternative explanation of the local maximum at -1.5 on the x-axis in the histogram in Fig. 17 for both long and short GRBs, however, a more in-depth study has been conducted in the appendix (see section. 7.1) to study this alternative explanation. This study indicates that this is not a likely explanation and further motivates the photon count cut-off of 15% of the probable prompt emission for the precursor emission period.

An overview of the photon count for the precursor phase and prompt emission before and after applying the photon count selection criterion can be seen in Fig. 18 for long GRBs and Fig. 19 for short GRBs. As can be seen in both distributions after the selection, the selection has removed the first emission period high photon count GRBs.

4.7 Precursor Validation

After applying these criteria on the GRB trigger signals from the GBM, it is noted that for a single GRB, various observations with different instruments do not always display the same findings. Some indicated the presence of a precursor whereas others did not for the same GRB. This is likely due to fluctuations in the observed background rate.

To account for possible fluctuations in the observed background photon rate, a precursor is only validated if it is observed by at least two instruments from the GBM. If both instruments have detected the precursor, as for example seen in Fig. 20, the GRB is validated. This last verification step concludes the precursor selection. The statistics of the resulting sample will be discussed in section 5.1.

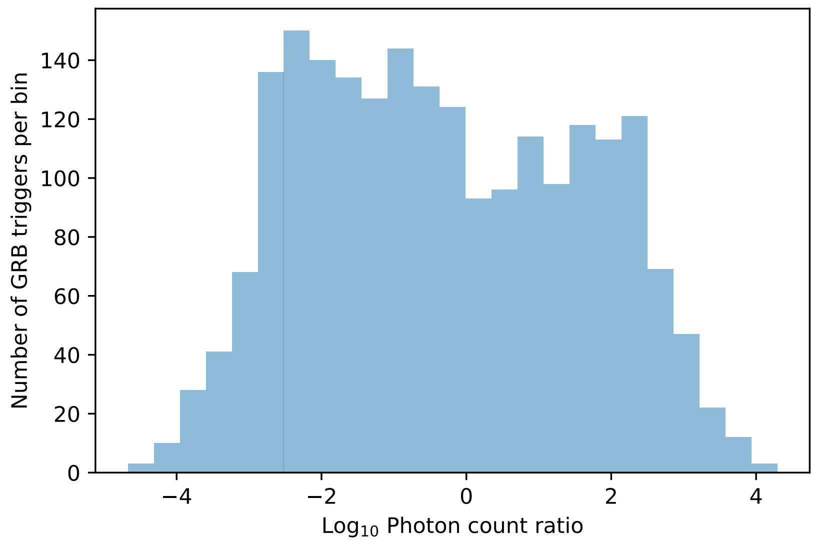

(a) Long GRBs

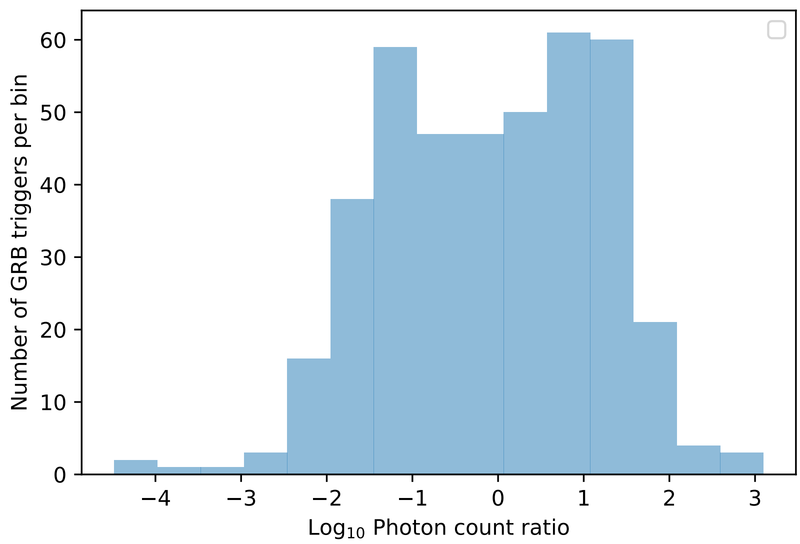

(b) Short GRBs

Figure 17: The distribution of the photon count ratio for long and short GRBs.

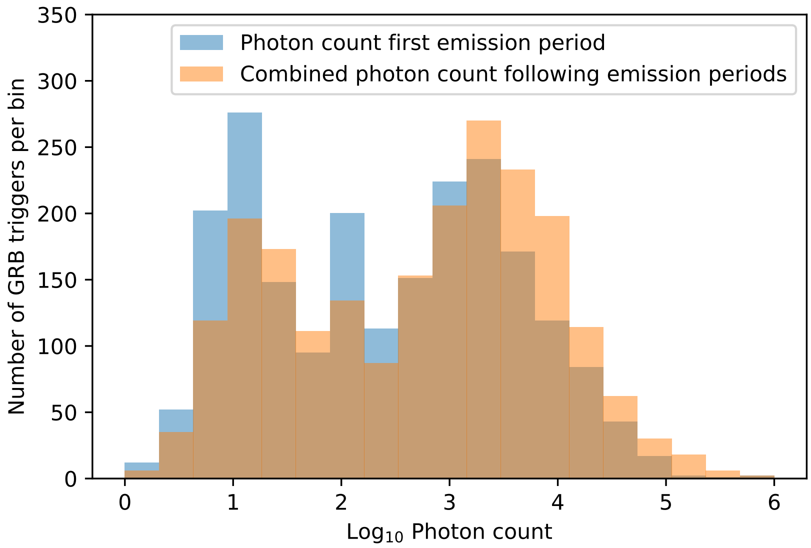

(a) Long GRBs - Before criterion

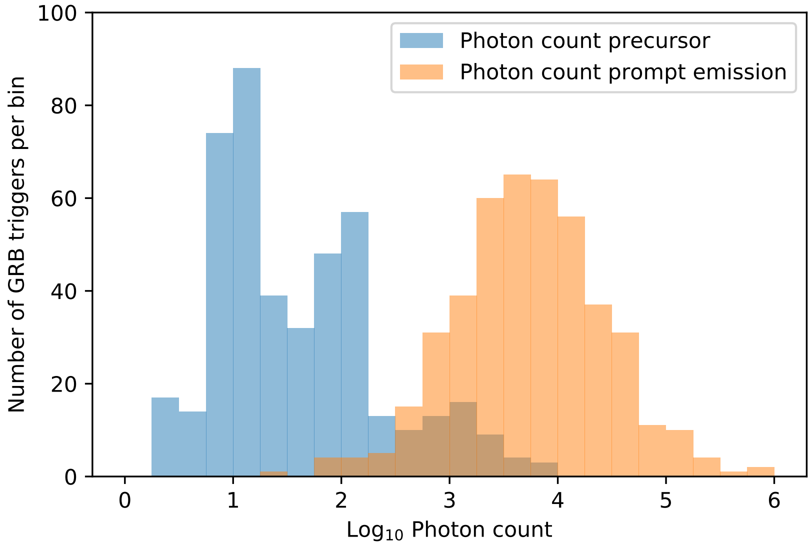

(b) Long GRBs - After criterion

Figure 18: Photon count distribution for long GRBs before and after applying the photon count criterion.

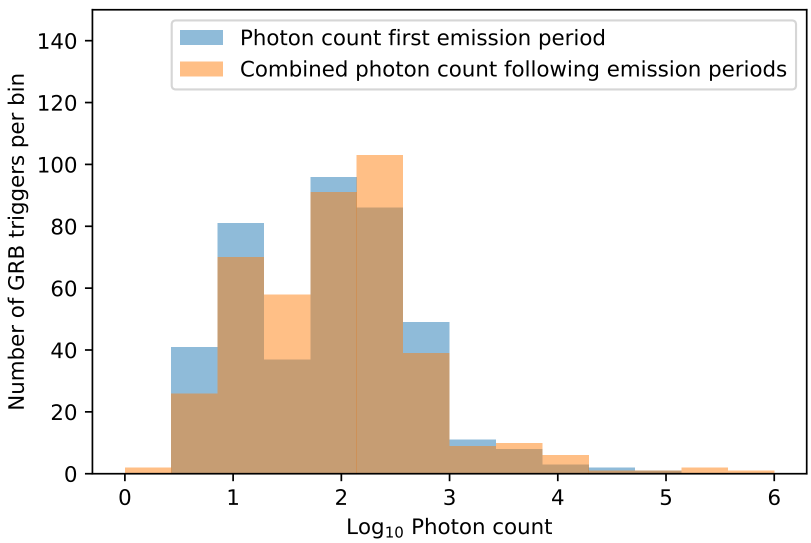

(a) Short GRBs - Before criterion

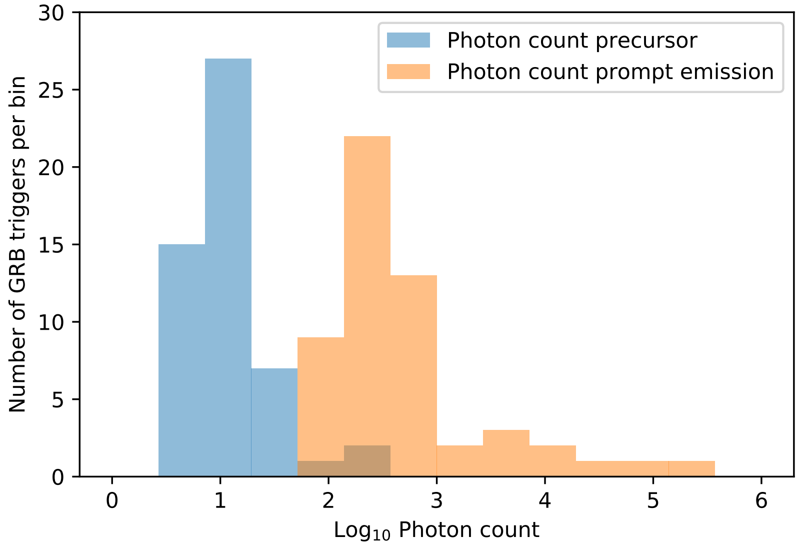

(b) Short GRBs - After criterion

Figure 19: Photon count distribution for short GRBs before and after applying the photon count criterion.

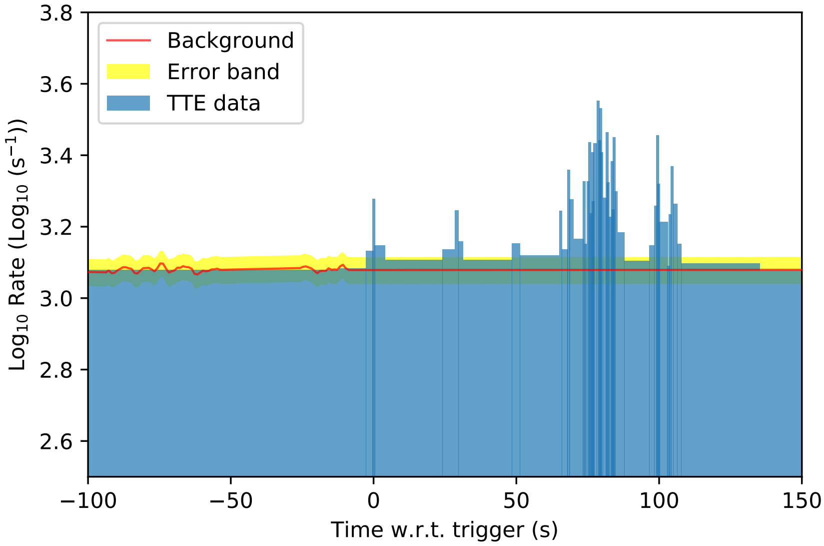

(a) Instrument n7

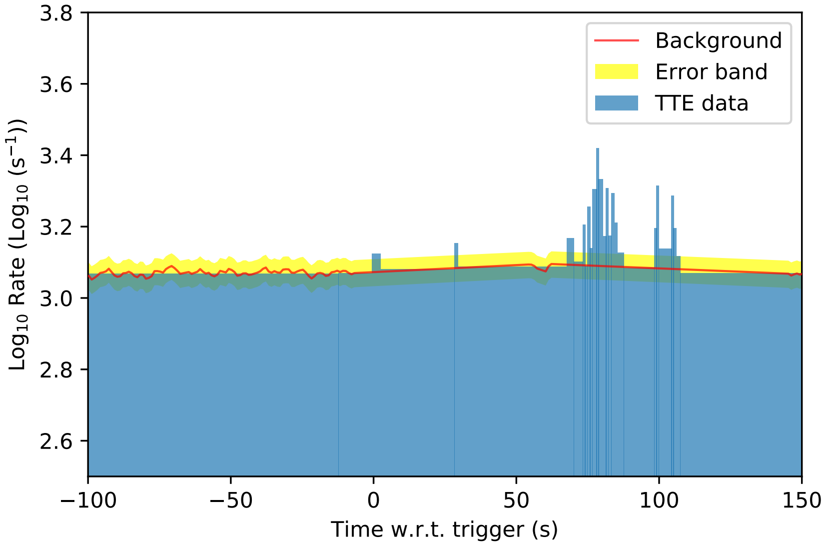

(b) Instrument n8

Figure 20: The Bayesian block algorithm applied to the TTE and CTIME data and the interpolated background from the CTIME data as detected by instruments n7 and n8 of the GBM for GRB trigger bn141029134.

5 Precursor Time Window Analysis

The goal of this thesis is to determine the temporal properties of the precursor phase in order to define an extended neutrino production window for neutrino observations by the IceCube Neutrino Observatory. The dense medium surrounding the progenitor in the precursor phase of GRBs in some of the precursor models should be an ideal environment for an increased neutrino production.

A GRB sample containing probable precursors has been carefully selected from several years of data recorded by the Fermi GBM based on two criteria. The temporal properties of this precursor sample determined in this thesis can be used in subsequent analyses by the IceCube Collaboration. A follow-up study of the correlation between these temporal properties of precursors and the arrival times of neutrinos recorded by IceCube might shed light on the existence of neutrinos and UHECRs produced in GRBs during the precursor window. If there are no GRB neutrinos detected during the extended neutrino production window as defined by the temporal properties of the precursors, further constraints on the likeliness of GRBs as the mechanisms behind high-energy neutrinos and UHECRs can be determined.

In order to find GRB neutrinos there are two main methodologies which might be applied. A first methodology can use the individual temporal properties of each precursor as defined in this thesis. For each precursor, the most inclusive time interval of precursor activity T_{100} and the exact start and end times of this interval are recorded. For each detected precursor there is a temporal window using the start and end of these periods for neutrino searches. If a neutrino is detected during this time interval, it can be checked whether the direction of origin agrees with the location of the GRB. The statistics of these temporal properties will be discussed in section 5.1

The second possibility for subsequent neutrino searches could be achieved by a general characterization of the temporal properties of the precursor window w.r.t. the start of the prompt emission. An appropriate upper limit for the duration of the quiescent period between the precursor and the prompt emission and an appropriate upper limit for the duration of the precursors in precursor GRBs would allow for the definition of a maximal time window in which most precursors are located. Using a stacking analysis of neutrino detections, it would then be possible to observe if an increase in neutrino observations is present during this window.

5.1 Precursor Statistics

The initial GRB sample contained 1545 long GRBs and 309 short GRBs. After applying the selection criteria it was found that 212 long GRBs and 26 short GRBs contained precursors. In this study, it is thus found that approx. 13.7% of long GRBs and 8.4% of short GRBs contain precursors.

As seen earlier in both the mechanisms and observations of precursors, the properties of long and short GRBs are different. Therefore a separate analysis for both has been developed. For each precursor and prompt emission period, the most inclusive time intervals T_{100} have been determined. The distribution of this property can be seen in Fig. 21. It is noted that the duration of prompt emission is generally longer than the duration of the precursor, as is expected. This can also be observed from the distribution of the ratio of the T_{100} of the precursor and the prompt. As can be seen in Fig. 22, the ratio is consistently smaller than 1, indicating that the precursor period is consistently shorter than the prompt period. Aside from this, a peculiar feature of these distributions is noted. Both the distributions for the long and short GRBs are bimodal.

One can determine an upper limit on the length of the precursor phase T_{100}. The 90th percentile P_{90} of T_{100} for long GRBs is found to be 2.9 s whereas the 90th percentile P_{90} of T_{100} for short GRBs is 0.5 s. The distributions hereof can be seen in Fig. 23.

The distribution of the duration of the quiescent period T_Q between the precursor and prompt emission can be seen in Fig. 24. Whereas most long and short GRB's quiescent periods are under 100 s, a significant amount of longer quiescent periods are present. The distribution ends at approx. 600s as this is the maximum time in which the search algorithm for emission periods has been applied.

One can determine an upper limit on the quiescent period between the precursor and prompt emission by determining the 90th percentile P_{90} of the quiescent period distribution. This is done for both short and long GRBs. For short GRBs it is found that $P_{90}(T_Q) = 115.1$ s whereas for long GRBs $P_{90}(T_Q) = 291.9$ s. This is illustrated in the distributions in Fig. 25.

More statistics on the resulting precursor sample can be found in the appendix 7.2.

5.2 Extended Neutrino Production Time Window

The statistics detailed in the previous section can be used to define an extended neutrino production time window as this is directly correlated with the examined precursor time window. This can be done for each precursor observation individually by using the time interval in which the precursor is active, as determined in this thesis. Seeking for neutrino observations in the precursor window of a GRB might lead to a direct identification of a neutrino originating from this GRB.

However, a second possibility is a stacking analysis of observed neutrino signals during time intervals containing observed GRBs. If one synchronizes the observed neutrino signals for each time interval by overlapping the start of the prompt emission of the GRB in these intervals, an increase of observed neutrinos during an extended neutrino time

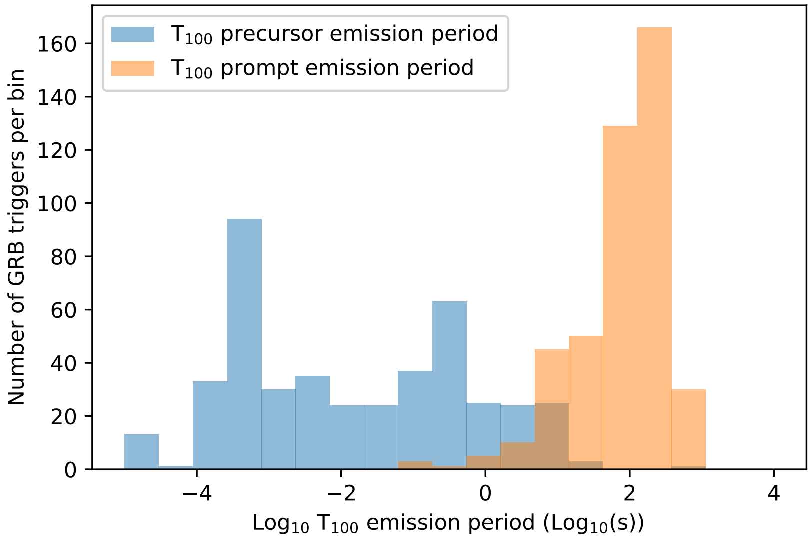

(a) Long GRBs

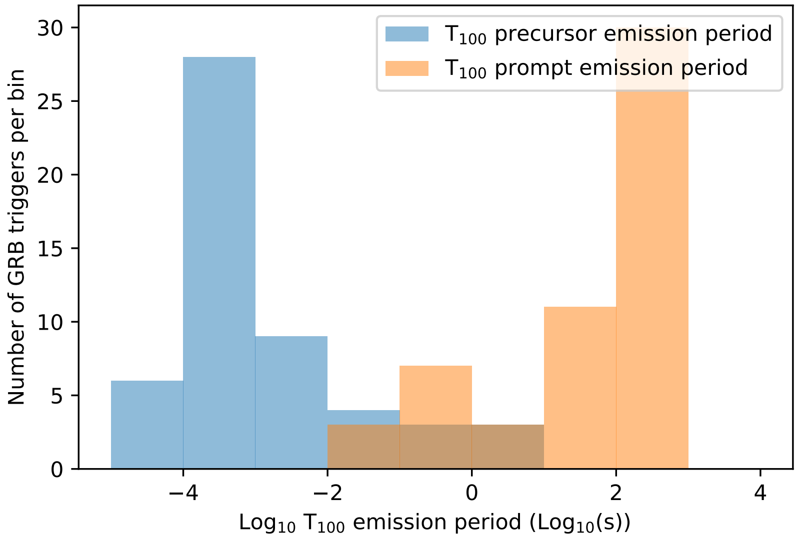

(b) Short GRBs

Figure 21: T_{100} distribution for both the precursor phase and prompt emission for long and short GRBs.

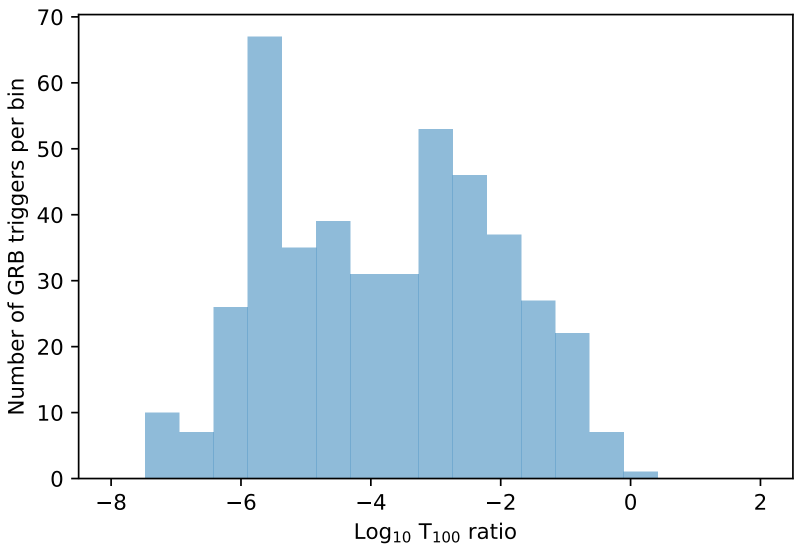

(a) Long GRBs

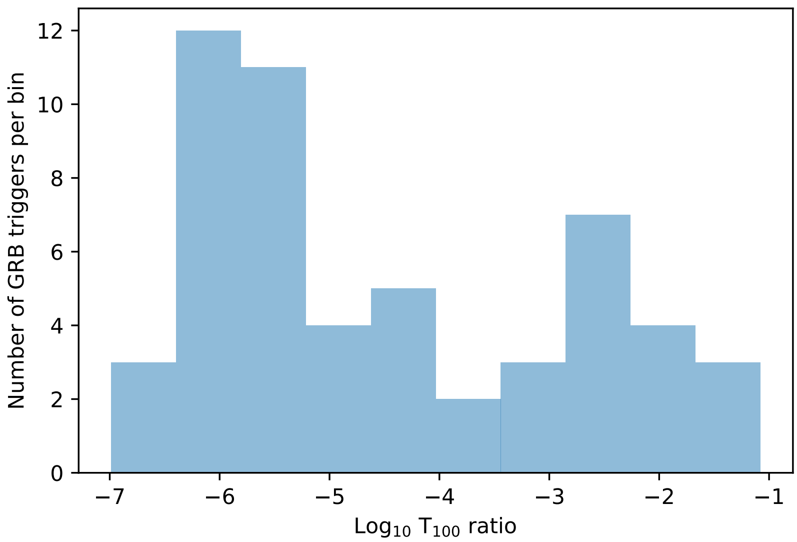

(b) Short GRBs

Figure 22: Distribution of the ratio of precursor T_{100} and prompt T_{100} for long and short GRBs.

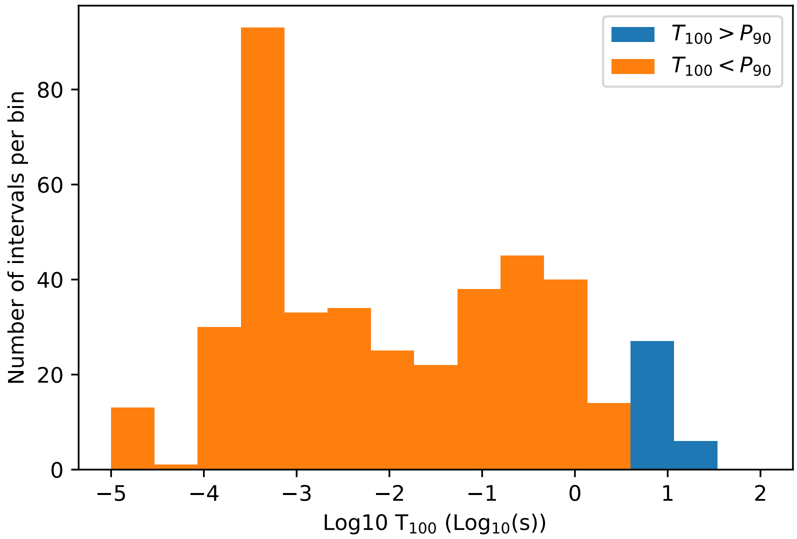

(a) Long GRBs, $P_{90}(T_{100}) = 2.9s$

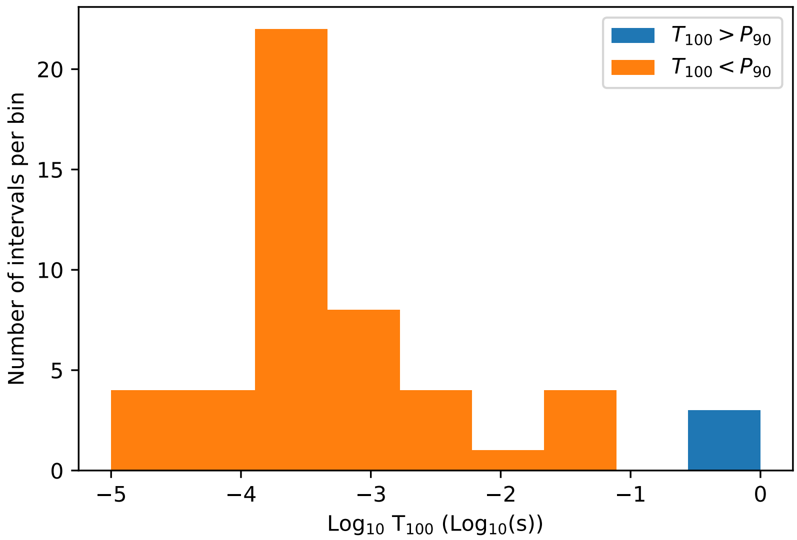

(b) Short GRBs, $P_{90}(T_{100}) = 0.5s$

Figure 23: T_{100} distribution the precursor phase of long and short GRBs.

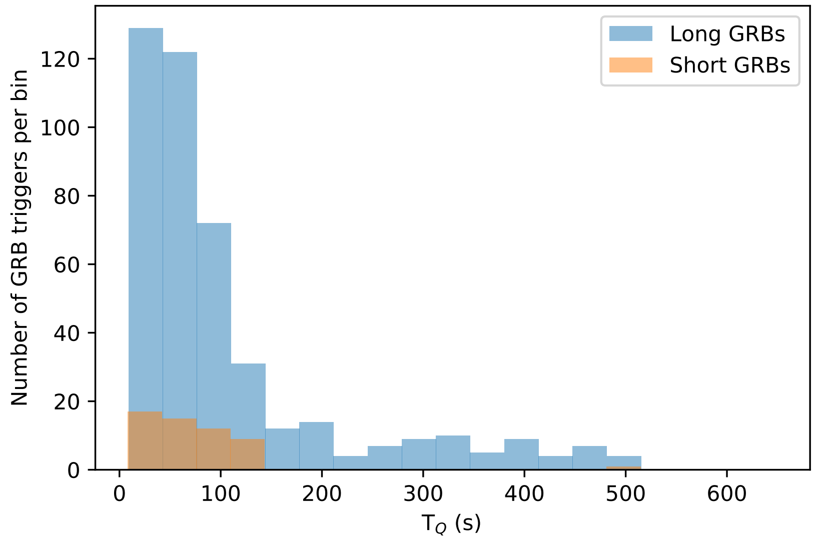

Figure 24: The distribution of the quiescent period T_Q between the precursor and prompt emission for long and short GRBs.

window characterized by the temporal precursor properties would validate an increased neutrino production during the precursor phase.

For long GRBs, it has been found that 90% of the GRBs have a quiescent period of less than 291.9 s and a precursor durations T_{100} of less than 2.9 s. In 90% of all short GRBs, the precursor has a quiescent period of less than 115.1 s and a precursor duration T_{100} of less than 0.5 s for 90% of the GRBs.

The sum of the quiescent period and precursor duration, or, the time interval between the start of the precursor and the start of the prompt emission ΔT_s is thus a key property in characterizing the precursor window. To determine an upper limit, one can take the 90th percentile P_{90} of ΔT_s. As such it is found that in 90% of long GRBs the precursor start $P_{90}(\Delta T_s) = 294.7$ s before the prompt emission. For short GRB this is $P_{90}(\Delta T_s) = 115.1$ s before the prompt emission. An overview hereof can be seen in Fig. 26. This precursor characteristic uniquely defines a maximal time window in which 90% of the precursors are located for all precursor GRBs. A neutrino stacking analysis revealing an increased neutrino observation rate in this maximal time window would thus indicate an increased neutrino production during precursors.

To get a better understanding of the window in which neutrinos are likely to be observed, a bivariate kernel density estimate of the period between the start of T_{100} of the precursor and the start of T_{100} of the prompt (ΔT_s) and the period between the end of T_{100} of the precursor and the start of T_{100} of the prompt (ΔT_e) for short and long

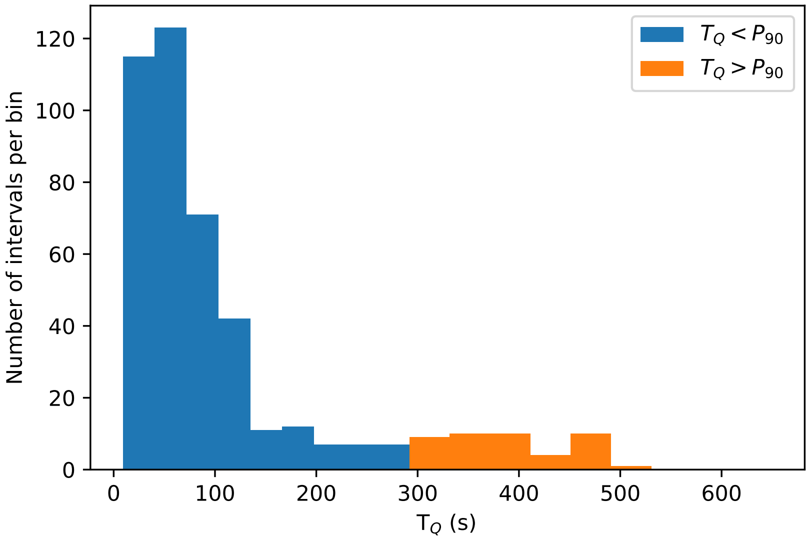

(a) Long GRBs, $P_{90}(T_Q) = 291.9s$

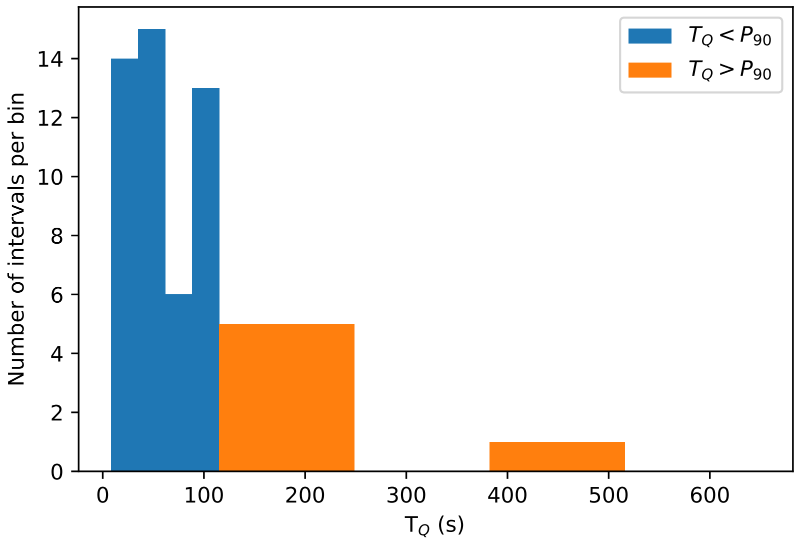

(b) Short GRBs, $P_{90}(T_Q) = 115.1s$

Figure 25: Distribution of T_Q of long and short GRBs.

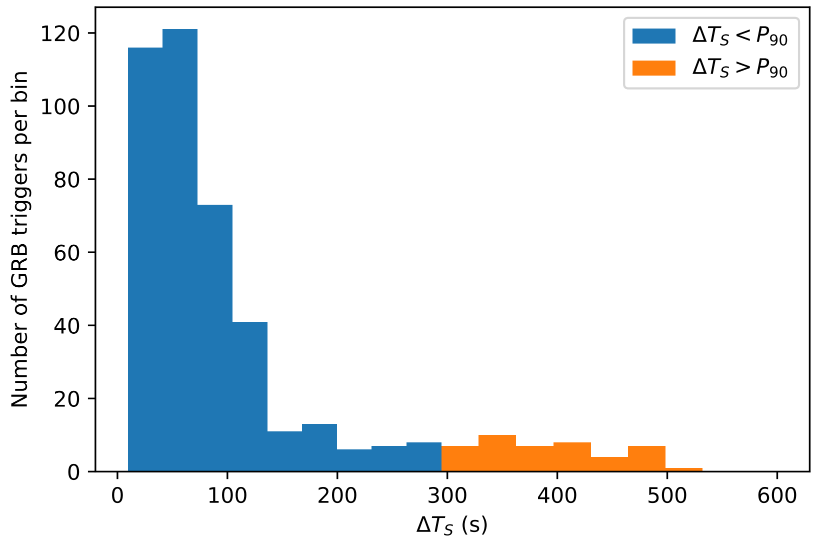

(a) Long GRBs, $P_{90} = 294.7$ s

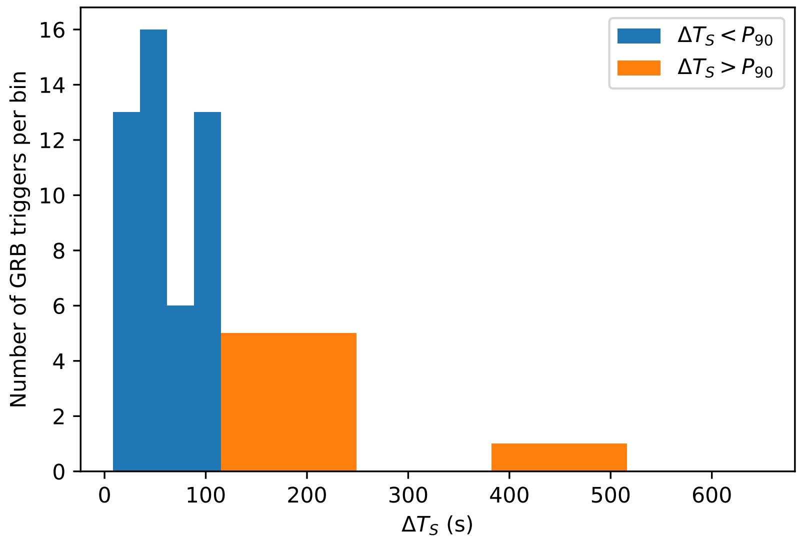

(b) Short GRBs, $P_{90} = 115.1$ s

Figure 26: Time interval between the start of the precursor and the start of the prompt emission ΔT distribution for long and short GRBs.

GRBs has been made. Given a collection of observed neutrinos at times t before the prompt emission of (different) GRBs, one can then compare the probability density of the bivariate kernel density with the observed neutrino density and seek for correlations. See Fig. 27 for the bivariate kernel density estimates. This kernel density estimate indicates regions with high probability density for the start and end of precursors, if a correlation of these regions exists with the observations of neutrinos, one could indicate precursors as periods of increased neutrino production in GRBs.

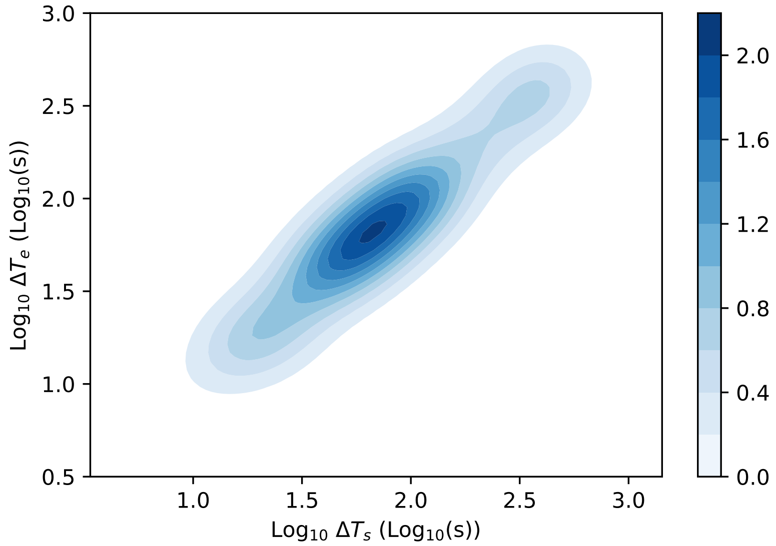

(a) Long GRBs

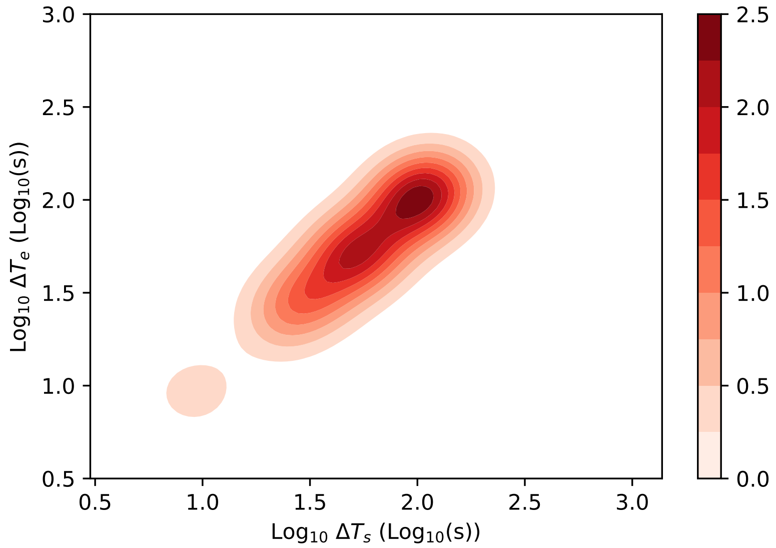

(b) Short GRBs

Figure 27: Bivariate kernel density estimate for ΔT_s and ΔT_e for long and short GRBs.

6 Conclusion

To date, no gamma-ray burst neutrinos have been observed to a high significance during the dominant or prompt emission of GRBs. As precursors models predict the central engine to be surrounded by a dense medium (e.g. the stellar envelope in the shock break-out precursor and fallback precursor models) during the precursor phase, an increased neutrino production is expected to take place due to e.g. interactions of the jet with this medium. As no significant neutrino signals have been observed coincident with the prompt phase, a wider temporal window will be examined. The focus of this thesis is thus to determine an extended neutrino production time window based on the temporal properties of the precursors.

To obtain this extended time window one needs to identify the individual emission periods within a GRB. To do this, it is needed to model the background to be able to discern any relevant GRB emission from the present background signal. Several methodologies have been examined. The most robust background model has been applied to identify individual emission periods within a GRB from the CTIME and TTE data from the Gamma-ray Burst Monitor instruments with the use of the Bayesian block algorithm. Once the emission periods were identified, several criteria (inspired by various previous studies on this topic) were examined and applied to select precursors from the GRB sample. A final sample was created by demanding the precursor to be detected in at least two GRB triggers observed by different instruments of the GBM.

The findings in this thesis of the final precursor sample indicate that 13.7% of long GRBs and 8.4% of short GRBs contain precursors. Although the exact percentages vary among studies due to different precursor definitions and methodologies applied, these numbers are roughly consistent with the findings of earlier studies. It is noted that short GRBs consistently contain fewer precursors than their long counterpart in various population studies. This is the case in our findings as well, which reinforces the belief in the robustness of the applied methodology.

The detailed temporal statistics gathered for every precursor GRB in this thesis allow for an individual search for recorded neutrinos by the IceCube Neutrino Observatory during the precursor windows. This individual approach allows for the correlation between the observed neutrinos with a certain GRB.

A second analysis could be done in the form of a stacking analysis of observed neutrino signals. After an examination of the temporal properties of the precursor sample, several statistics characterizing a precursor window have been established. It has been found that 90% of GRBs have a quiescent period of less than 291.9 s for long GRBs and 115.1 s for short GRBs. Precursor GRBs have a precursor duration T_{100} of less than 2.9 s for long GRBs and 0.5 s for short GRBs in 90% of the cases. The sum of the quiescent period and precursor duration ΔT_s is the key property in characterizing the precursor window. It is found that in 90% of long GRBs the precursor start $P_{90}(\Delta T_s) = 294.7$ s before the prompt emission. For short GRB this is $P_{90}(\Delta T_s) = 115.1$ s before the prompt emission. If an increase of observed neutrinos with the IceCube Neutrino Observatory is present during this maximal time window in which 90% of the precursors are located, this could indicate the existence of GRB neutrinos.

Given the statistics of various properties of (precursor) GRBs generated by this study, further examination of the generated data might uncover leads to the mechanisms responsible for the precursors. For example, for long GRBs, the distributions of the ratio of the T_{100} of precursors and the prompt emission (see Fig. 22) indicate a bimodal distribution whereas the distribution of the T_{100} of the prompt emission (see Fig. 21) does not display any bimodality. These two local maxima in the ratio distribution might indicate the presence of two different precursor mechanisms. However, further research should be conducted to confirm this. Additional statistics on the precursor sample have been added to the appendix.

In this study the goal to determine an extended neutrino production window has been established. Further research to seek GRB neutrinos using this extended window is able to be performed by the IceCube Collaboration and the provided statistics by this study might be used in future research to examine precursor mechanisms.

7 Appendix

7.1 Study of the Photon Count Criterion

When examining the ratio of the integrated photon count of the precursor and the prompt in Fig. 17, it is noted that an alternative explanation for the local maximum at -1.5 on the x-axis is possible. Due to the fact that in GRBs which have more than two emission periods the probable prompt phase contains more than one emission period, it is logical to assume that this probable prompt phase contains more photons than the probable precursor (which is the first emission period in the prompt in case it is not validated as a precursor emission period by the criteria).

The ratio in this distribution is defined as,

$$r = \frac{n_{\text{Probable precursor}}}{n_{\text{Probable prompt}}}, \tag{18}$$

where r indicates the ratio and n the integrated photon counts. To account for the effects for multiple emission periods in the probable prompt the following ratio was examined

$$r = \frac{n_{\text{Probable precursor}}}{\frac{n_{\text{Probable prompt}}}{N}}, \tag{19}$$

where N is the number of emission periods in the probable prompt. This ratio between the photon count in the probable precursor and the average photon count of an emission period in the probable prompt eliminates the potential biased effects discussed earlier.

The distribution of this adapted ratio can be seen in Fig. 28. These distributions further motivate the 15% criterion.

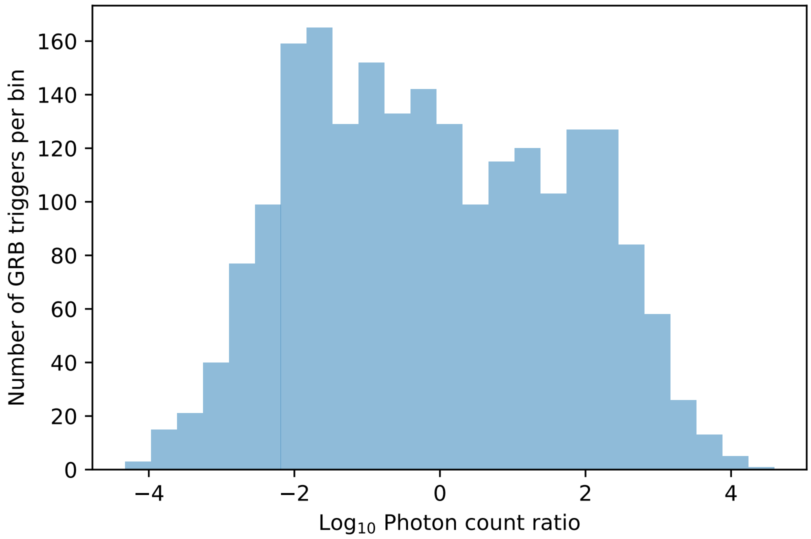

(a) Long GRBs

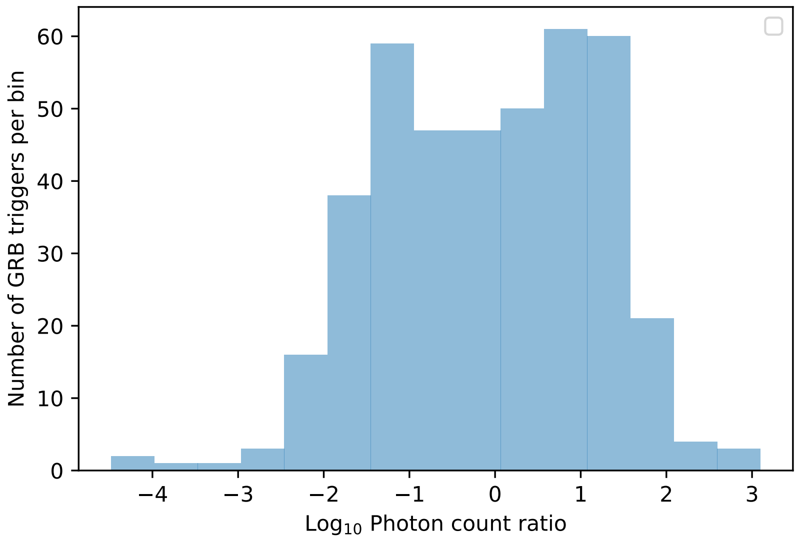

(b) Short GRBs

Figure 28: The distribution of the adapted photon count ratio for long and short GRBs.

7.2 Additional Precursor Statistics

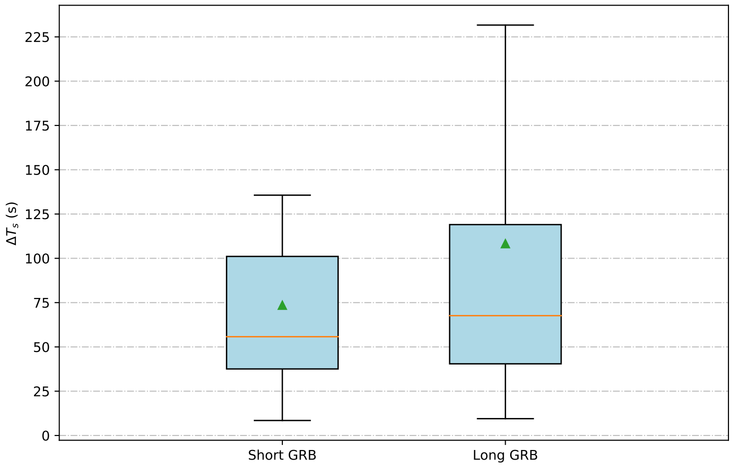

Figure 29: Boxplots displaying ΔT_s, the period between the start of T_{100} of the precursor and the start of T_{100} of the prompt for short and long GRBs. The vertical orange line displays the median, whereas the green triangle displays the mean.

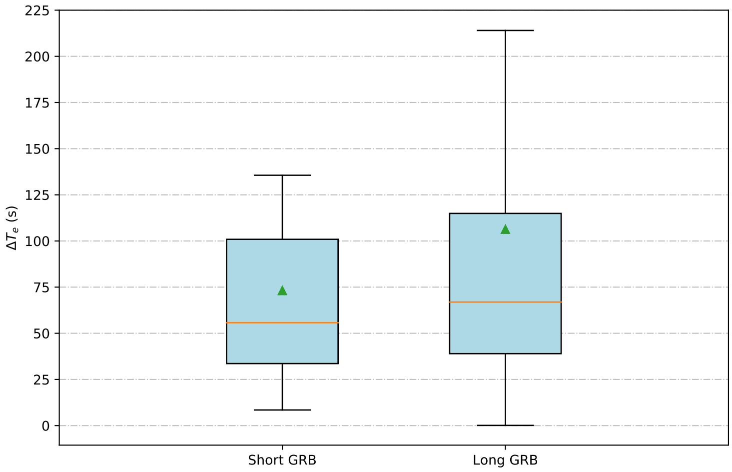

Figure 30: Boxplots displaying ΔT_e, the period between the end of T_{100} of the precursor and the start of T_{100} of the prompt for short and long GRBs. The vertical orange line displays the median, whereas the green triangle displays the mean.

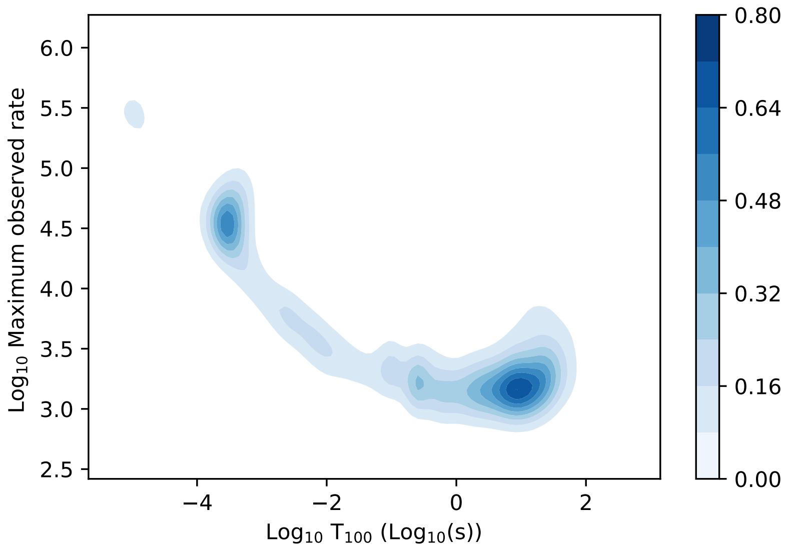

(a) Precursor KDE - Long GRBs

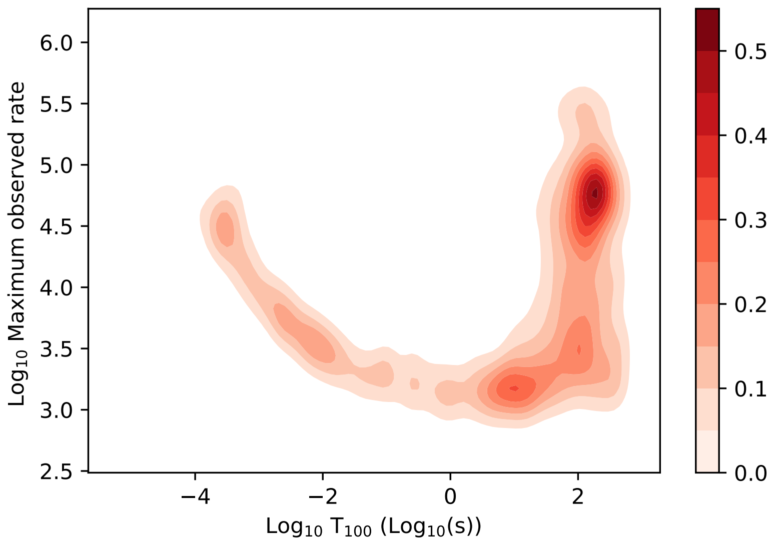

(b) Prompt KDE - Long GRBs

Figure 31: Bivariate kernel density estimate for T_{100} and the maximum observed photon count for the precursor and prompt for long GRBs before applying the criteria.

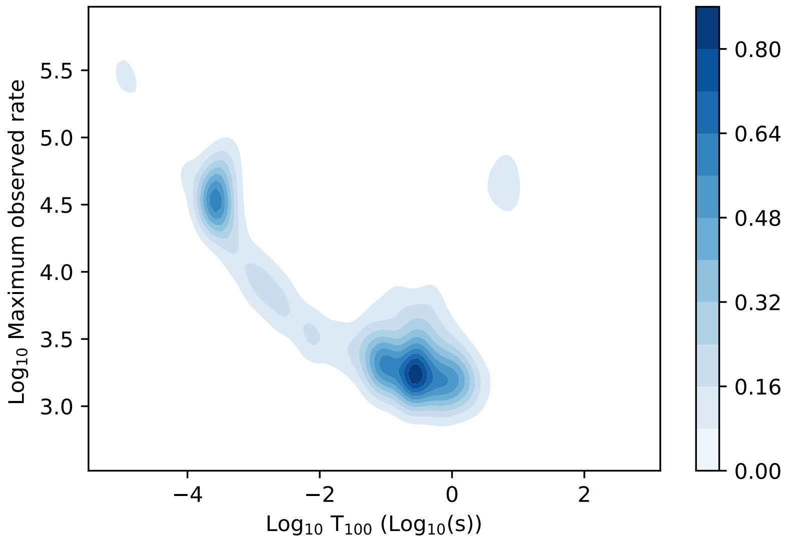

(a) Precursor KDE - Short GRBs

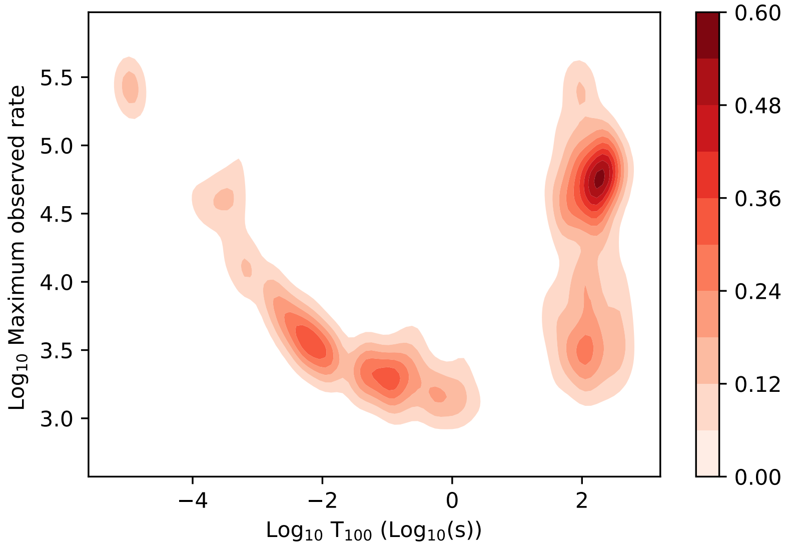

(b) Prompt KDE - Short GRBs

Figure 32: Bivariate kernel density estimate for T_{100} and the maximum observed photon count for the precursor and prompt for short GRBs before applying the criteria.

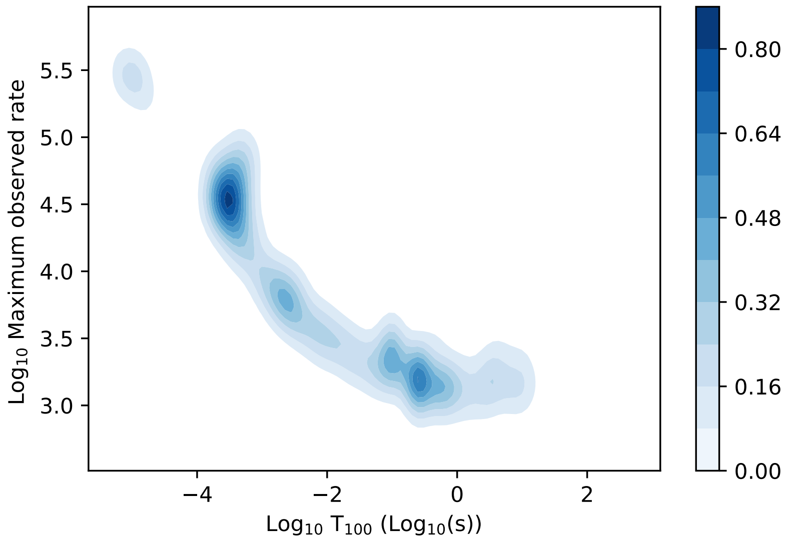

(a) Precursor KDE - Long GRBs

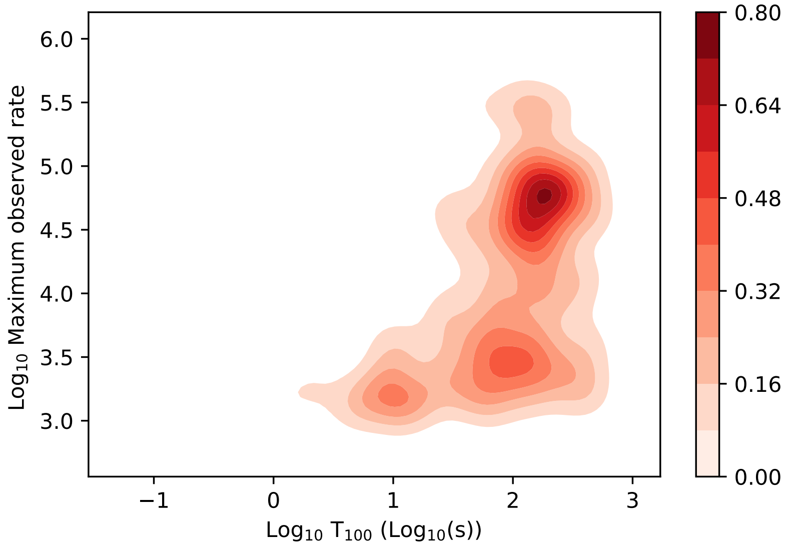

(b) Prompt KDE - Long GRBs

Figure 33: Bivariate kernel density estimate for T_{100} and the maximum observed photon count for the precursor and prompt for long GRBs after applying the criteria.

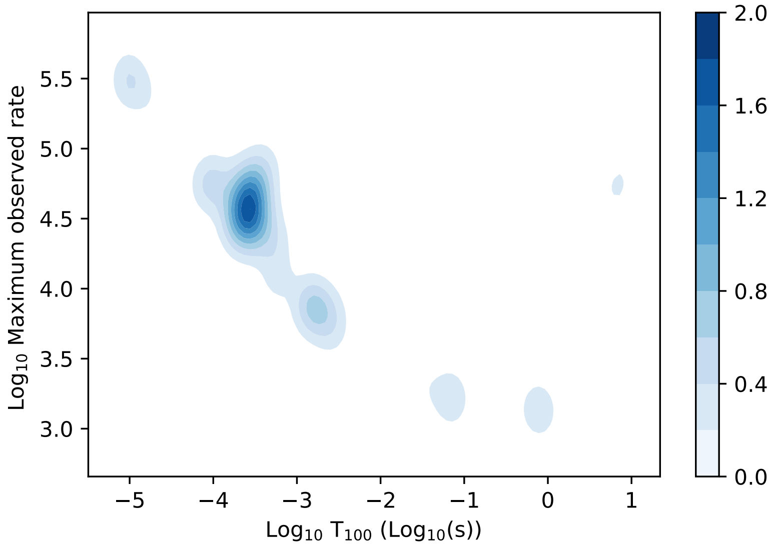

(a) Precursor KDE - Short GRBs

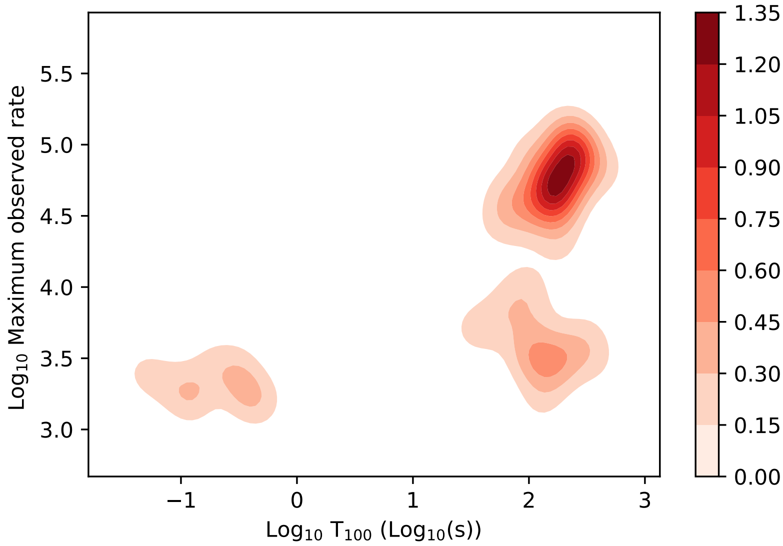

(b) Prompt KDE - Short GRBs

Figure 34: Bivariate kernel density estimate for T_{100} and the maximum observed photon count for the precursor and prompt for short GRBs after applying the criteria.

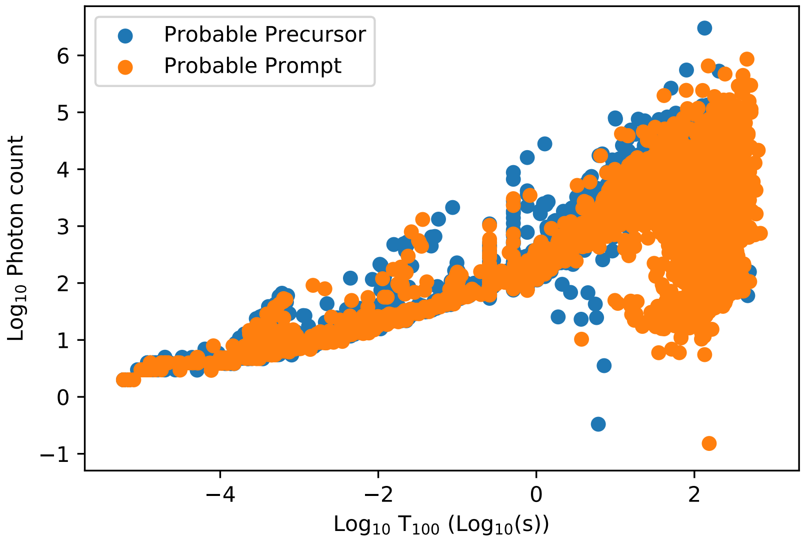

(a) Long GRBs

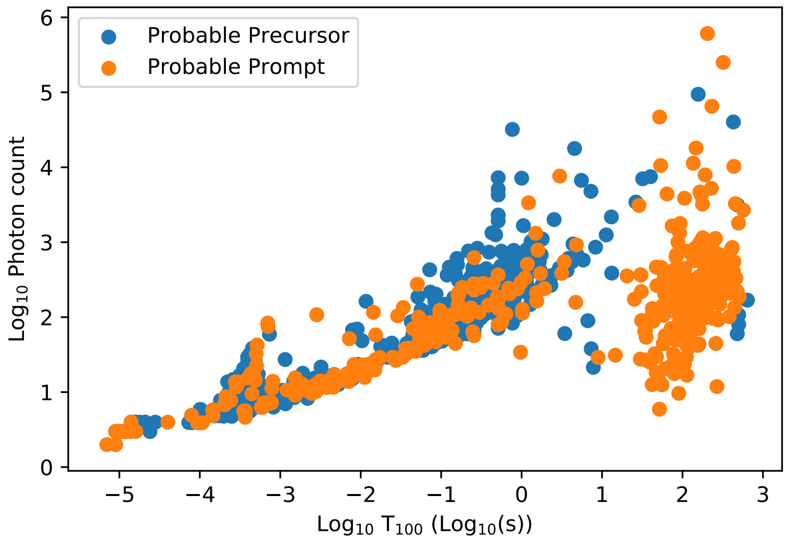

(b) Short GRBs

Figure 35: Scatter plot of T_{100} and the integrated photon count for the precursor and prompt for long and short GRBs before applying the criteria.

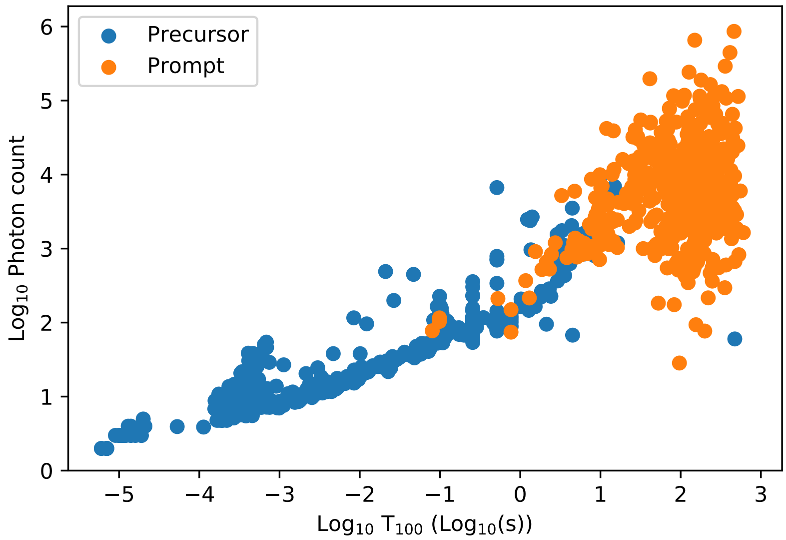

(a) Long GRBs

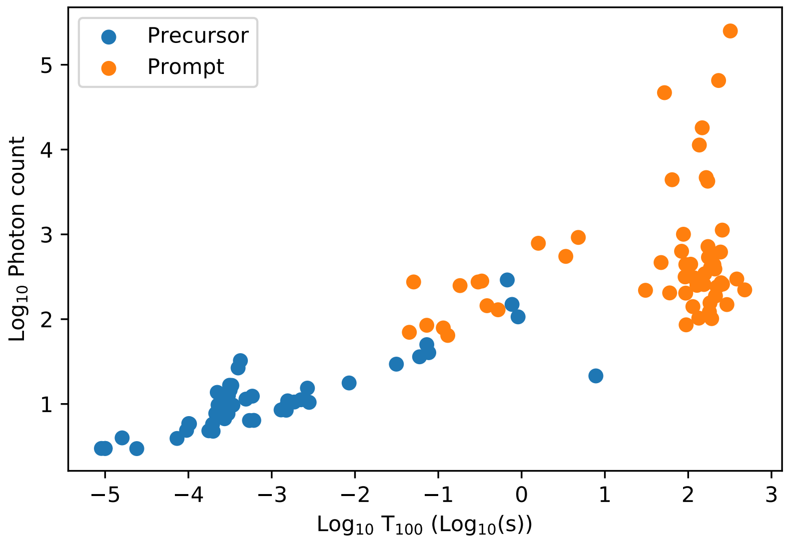

(b) Short GRBs

Figure 36: Scatter plot of T_{100} and the integrated photon count for the precursor and prompt for long and short GRBs after applying the criteria.

References

[1] Dawson B.R., et al., *Past, Present and Future of UHECR Observations*, 2017. Available at arXiv: 1703.07897

[2] Wang F., *A Comprehensive Statistical Study On Gamma-Ray Bursts*, 2019. Available at arXiv: 1902.05489

[3] Asano K., Murase K. *Gamma-Ray Bursts as Multienergy Neutrino Sources*, 2015. DOI: `http://dx.doi.org/10.1155/2015/568516`

[4] ANTARES Collaboration, *The ANTARES Collaboration: contributions to the 31st International Cosmic Ray Conference (ICRC 2009), Lodz, Poland, July 2009*, 2010. Available at arXiv: 1002.0701

[5] IceCube Collaboration, *An All-Sky Search for Three Flavors of Neutrinos from Gamma-Ray Bursts with the IceCube Neutrino Observatory*, 2016. Available at arXiv: 1601.06484

[6] LIGO Scientific Collaboration, Virgo Collaboration, Fermi Gamma-Ray Burst Monitor, INTEGRAL, et al., *Multi-messenger Observations of a Binary Neutron Star Merger*, 2017. Available at arXiv: 1710.05833

[7] Fermi-LAT Collaboration, *Fermi-LAT observations of the LIGO/Virgo event GW170817*, 2017. Available at arXiv: 1710.05450

[8] IceCube Collaboration, Fermi-LAT, MAGIC, et al., *Multimessenger observations of a flaring blazar coincident with high-energy neutrino IceCube-170922A*, 2018. Available at arXiv: 1807.08816

[9] Bustamante M., et al., *High-energy cosmic-ray acceleration*, 2009. Available at: `https://cds.cern.ch/record/1249755/files/p533.pdf`

[10] Baerwald P., et al., *Are Gamma-Ray Bursts the Sources of the Ultra-High Energy Cosmic Rays?*, 2014. Available at arXiv: 1401.1820

[11] IceCube Collaboration, *An Absence of Neutrinos Associated with Cosmic Ray Acceleration in Gamma-Ray Bursts*, 2013. Available at arXiv: 1204.4219

[12] Sigl G., *High Energy Neutrinos and Cosmic Rays*. 2012. Available at arXiv: 1202.0466v1.

[13] Michelson P.F., Atwood W.B., Ritz S., *Fermi Gamma-ray Space Telescope: High-Energy Results from the First Year*, 2010. Available at arXiv: 1011.0213

[14] Gupta M., *Calculation of radiation length in materials*, 2010. Available at: `https://cds.cern.ch/record/1279627?ln=en`

[15] Fermi-LAT Collaboration, Atwood W.B., *The Large Area Telescope on the Fermi Gamma-ray Space Telescope Mission*, 2009. Available at arXiv: 0902.1089

[16] Meegan C., et al., *The Fermi Gamma-Ray Burst Monitor*, 2009. Available at arXiv: 0908.0450

[17] IceCube Collaboration, *IceCube Explained*, s.d. [Online, accessed May 26, 2016]. Available at `https://icecube.wisc.edu/about/overview`

[18] IceCube Collaboration. *The IceCube Neutrino Observatory: Instrumentation and Online Systems*, 2017. Available at arXiv: 1612.05093v2

[19] Jero K., *Reconstruction Introduction*, 2015. Available at: `https://icecube.wisc.edu/~kjero/Bootcamp/2015/Notebooks/Reconstruction_Introduction.html`

[20] Minamizaki A., *A window into the Earths interior*, s.d. [Online, accessed May 26, 2016]. Available at `http://www.u-tokyo.ac.jp/en/utokyo-research/feature-stories/a-window-into-the-earths-interior/`

[21] Cofield C., *IceCube catches high-energy neutrino oscillations*, Nature, 2012, DOI:10.1038/nature.2012.10776.

[22] Van Eijndhoven N., *Experimental Study of the Microcosmos and Macrocosmos.* Lectures Vrije Universiteit Brussel (VUB), 2016. Available at: `http://sites.google.com/site/nickveweb`

[23] IceCube Neutrino Observatory, *Air showers in IceCube: Analysis of data from IceCube and IceTop*, Nucl. Phys. B., **175**, 2007, p. 415. DOI: 10.1016/j.nuclphysbps.2007.11.042.

[24] Bravo S., *Designing the future of the IceCube Neutrino Observatory*, 2014. Available at arXiv: 1412.5106v2.

[25] Gaisser T. *Cosmic rays and particle physics*,1979. DOI: 10.1017/CBO9781139192194

[26] Griffiths D.J., *Introduction to elementary particles.* Weinheim: WHILY-VCH, 2008.

[27] IceCube Collaboration. *The IceCube Neutrino Observatory, the Pierre Auger Observatory and the Telescope Array: Joint Contribution to the 34th International Cosmic Ray Conference (ICRC 2015)*, 2015. Available at arXiv: 1511.02109.

[28] LIGO Scientific Collaboration, Virgo Collaboration, Fermi Gamma-Ray Burst Monitor, INTEGRAL, *Gravitational Waves and Gamma-rays from a Binary Neutron Star Merger: GW170817 and GRB 170817A*. 2017. Available at arXiv: 1710.05834.

[29] Waxman E., *Cosmological Gamma-Ray Bursts and the Highest Energy Cosmic Rays.* Physical Review Letters, vol. 75, no. 3, pp. 386-389, 1995.

[30] Vietri M., *The acceleration of ultra-high-energy cosmic rays in gamma-ray bursts.* Astrophysical Journal Letters, vol. 453, no. 2, pp. 883-889, 1995.

[31] Paczynski B. and Xu G., *Neutrino bursts from gamma-ray bursts.* The Astrophysical Journal, vol. 427, no. 2, pp. 708-713, 1994.

[32] Gomboc A., *Unveiling the Secrets of Gamma Ray Bursts*, 2012. Available at arXiv: 1206.3127.

[33] Sari R., *Beaming and Jets in GRBs*, 2000. Available at arXiv: 0002165

[34] Baerwald P., Bustamante M., Winter W., *Are Gamma-Ray Bursts the Sources of the Ultra-High Energy Cosmic Rays?*, 2014. Available at arXiv: 1401.1820

[35] Dainotti M., Del Vecchio R., *Gamma Ray Burst afterglow and prompt-afterglow relations: an overview*, 2017. Available at arXiv: 1703.06876

[36] NASA's Goddard Space Flight Center. *NASA Sees 'Watershed' Cosmic Blast in Unique Detail*, 2013. Available at: `https://www.nasa.gov/content/goddard/nasa-sees-watershed-cosmic-blast-in-unique-detail`

[37] Lazzati D., *GRB Progenitors and Environment*, 2005. Available at arXiv: astro-ph/0505044

[38] Sari R., Piran T., *Variability in GRBs - A Clue*, 2018. Available at arXiv: 9701002

[39] Zhang B., Lu H., Liang E., *GRB Observational Properties*, 2016. Available at arXiv: 1611.01948

[40] Li Y., Zhang B., Lu H., *A Comparative Study of Long and Short GRBs. I. Overlapping Properties*, 2016. Available at arXiv: 1608.03383

[41] Mallozzi R.S., *BATSE GRB Durations*, 2018. Available at: `https://gammaray.msfc.nasa.gov/batse/grb/duration/`

[42] Meegan C.A., et al., *Identification of two classes of Gamma-Ray Bursts*, 1993. DOI: 10.1086/186969

[43] Pols O.R., Nomoto K., *Close binary progenitors of type Ib/Ic and IIb/II-L supernovae*, ASP Conference Series, Vol. 130, p.153, 1997.

[44] Eldridge J.J., et al., *The death of massive stars - II. Observational constraints on the progenitors of type Ibc supernovae*, 2013. Available at arXiv: 1301.1975

[45] Zhu S., *Precursors in Gamma-Ray Bursts Observed by Fermi*, 2015. Available at DRUM: `https://doi.org/10.13016/M2CH9N`

[46] Matsuura M., *The mass-loss rates of red supergiants at low metallicity: Detectionof rotational CO emission from two red supergiants in the LargeMagellanic Cloud*, 2015. Available at arXiv: 1608.01729

[47] Metzger B.D., *Kilonovae*, 2016. Available at arXiv: 1610.09381

[48] Cowan J.J., et al., *Making the Heaviest Elements in the Universe: A Review of the Rapid Neutron Capture Process*, 2019. Available at arXiv: 1901.01410.

[49] Tanvir N.R., et al., *A "kilonova" associated with short-duration gamma-ray burst 130603B*, 2013. Available at arXiv: 1306.4971

[50] Janiuk A., Sapountzis K., *Gamma Ray Bursts. Progenitors,accretion in the central engine, jet acceleration mechanisms*, 2018. Available at arXiv: 1803.07873

[51] Dainotti M.G., Del Vecchio R., *Gamma ray bursts afterglow and prompt afterglow relations: an overview*, 2017. Available at arXiv: 1703.06876

[52] Wang X.-Y., Meszaros P., *GRB Precursors in the Fallback Collapsar Scenario*, 2007. Available at arXiv: 0702441

[53] Piran T., *Gamma-Ray Bursts and the Fireball Model*, 1999. Available at arXiv:9810256

[54] Castro-Tirado A.J., *Observations and theoretical models of gamma-ray bursts*,2001. Available at arXiv: 0102122

[55] Beloborodov A.M., Meszaros P., *Photosperic Emission of Gamma-Ray Bursts*, 2017. Available at arXiv: 1701.04523

[56] Granot J., *The Structure and Dynamics of GRB Jets*, 2006. Available at arXiv: 0610379

[57] Cotter G., *High Energy Astrophysics*,2012. Available at: `http://www-astro.physics.ox.ac.uk/~garret/teaching/lecture3-2012.pdf`

[58] Hirata C., *1Cosmic Rays: I. General Phenomenology, Energy Loss, and Electromagnetic Signatures*, 2011. Available at: `http://www.tapir.caltech.edu/~chirata/ay102/CR.pdf`

[59] Lyutikov M., *The electromagnetic model of Gamma Ray Bursts*, 2005. Available at arXiv: 0512342

[60] Orienti M., et al., *The physics of the radio emission in the quiet side of the AGN population with the SKA.* 2014. Available at arXiv: 1412.5846.

[61] Zhang B., *Gamma-ray burst afterglows*, 2006. Available at arXiv: 0611774

[62] Lyutikov M., Usov V., *Precursors of gamma-ray bursts: a clue to the burster's nature*, 2000. Available at arXiv: 0007291

[63] Li L.-X., *Gamma-ray burst precursors as the remnant of the thermal radiation initially trapped in the fireball*, 2007. Available at arXiv: 0703144

[64] Zhang B., Yan H., *The internal-collision-induced magnetic reconnection and turbulence (ICMART) Model of Gamma-Ray Bursts*, 2018. Available at arXiv: 1011.1197

[65] Ramirez-Ruiz E., et al., *Precursors and electron-positron pair loading from erupting fireballs*, 2001. Available at arXiv: 0111342

[66] Murgula-Berthier A., et al., *Necessary Conditions for Short Gamma-Ray Burst Production in Binary Neutron Star Mergers*;2014. Available at arXiv: 1404.0383

[67] Wang X.-Y., Meszaros P., *GRB Precursors in the Fallback Collapsar Scenario*, 2007. Available at arXiv: 0702441

[68] Lipunov V., Gorbovskoy E., *Spinar Paradigm and Gamma Ray Bursts Central Engine*, 2008. Available at arXiv: 0706.3191

[69] Lipunov V. et al., *Discovery of the neutron stars merger GW170817/GRB170817a and Binary Stellar Evolution*, 2017. Available at arXiv: 1710.05911

[70] Penner A.J., et al., *Tidal deformations of neutron stars: The role of stratification and elasticity*, 2011. Available at arXiv: 1107.0669

[71] Tsang D., et al., *Resonant Shattering of Neutron Star Crusts*, 2011. Available at arXiv: 1110.0467

[72] Metzger A.E., et al., *Observation of a cosmic gamma-ray burst on Apollo 16*. Astrophys. Journal. pp194, 1974. DOI: 10.1086/181660.

[73] Koshut T.M., et al., *Gamma-Ray Burst Precursor Activity as Observed with BATSE*, Astrophys. Journal., V.452, pp. 145, 1995. DOI: 10.1086/176286.

[74] Burlon D., et al., *Time resolved spectral behavior of bright BATSE precursors*, 2009. Available at arXiv: 0907.5203

[75] Charisi M., et al., *Catalog of Isolated Emission Episodes in Gamma-ray Bursts from Fermi, Swift and BATSE*,2014. Available at ArXiv: 1409.2491

[76] Hogg D.W., *Data analysis recipes:Choosing the binning for a histogram*, 2008. Available at arXiv: 0807.4820.

[77] Scott D.W., *On optimal and data-based histograms*, Biometrika, Vol. 66, no. 3, pp. 605610, 1979.

[78] Freedman D., Daiconis P., *On the histogram as a density estimator: L2 theory*, Zeitschrift fr Wahrscheinlichkeitstheorie und Verwandte Gebiete, Vol. 57, no. 4, pp 453-476, 1981.

[79] Knuth K.H., *Optimal Data-Based Binning for Histograms*, 2006. Available at arXiv: 0605197

[80] Scargle J.D., *Studies in Astronomical Time Series Analysis.VI. Bayesian Block Representations*, 2012. Available at arXiv: 1207.5578

[81] Vanderplas J., *Bayesian Blocks for Histograms*. Available at: https://www.astroml.org/examples/algorithms/plot_bayesian_blocks.html

[82] Pollack B., et al., *Bayesian Blocks in High Energy Physics:Better Binning made easy!*, 2017. Available at arXiv: 1708.00810